MSc BioMedical Engineering

A patient-specific *in vitro* model for the study of metastatic bile duct cancer

Combining decellularization of metastatic locations with patient-derived cholangiocarcinoma organoids

Master thesis
Marije van Beek - 4442024

Faculty	:	Mechanical, Maritime, and Material Engineering (3mE)
Department	:	BioMechanical Engineering
Track	:	Medical Devices
Supervisors	:	Dr. ir. E.L. Fratila-Apachitei, Dr. M.M.A. Verstegen, MSc G.S. van Tienderen
Chair exam committee:		Prof. dr. A.A. Zadpoor
Date	:	28 February 2023

TU Delft Delft University of Technology

Table of Contents

List of abbreviations

AdvDMEM	Advanced dulbecco's modified eagle medium F12
BME	Basement membrane extract
CCA	Cholangiocarcinoma
CCAO	Cholangiocarcinoma organoids
dCCA	Distal cholangiocarcinoma
dECM	Decellularized extracellular matrix
dH_2O	Deionized water
dLECM	Decellularized lung extracellular matrix
DNA	Deoxyribonucleic acid
dNECM	Decellularized lymph node extracellular matrix
E	Young's modulus
eCCA	Extrahepatic cholangiocarcinoma
ECM	Extracellular matrix
EV	Extracellular vesicle
H&E	Hematoxylin and eosin
iCCA	Intrahepatic cholangiocarcinoma
O/N	Overnight
PBS	Phosphate-buffered saline
pCCA	Perihilar cholangiocarcinoma
PDX	Patient-derived xenograft
PFA	Paraformaldehyde
PSR	Picrosirius red
qPCR	Quantitative polymerase chain reaction
RNA	Ribonucleic acid
Rpm	Rotation per minute
SD	Standard deviation

Abstract

Cholangiocarcinoma (CCA) is a rare but aggressive type of primary liver cancer with a dismal prognosis. CCA commonly metastasizes to the lungs and lymph nodes, significantly reducing overall survival. However, a mechanistic understanding of how CCA invades these metastatic sites remains lacking. This is partly due to the failure of current models to recapitulate the complexity of tissue-specific environments for metastatic CCA. Patient-derived tumor organoids are promising models for studying cancer *in vitro*, including CCA. However, organoids are frequently cultured in basement membrane extract (BME), which does not represent the native microenvironment. Decellularized scaffolds can serve as a culture environment for investigating tumor-extracellular matrix (ECM) interactions. Nonetheless, decellularized scaffolds are often utilized in conjunction with cancer cell lines, lacking critical characteristics of a growing tumor *in vivo*. Therefore, this study aims to decellularize and characterize human-derived lung (n=3) and lymph nodes (n=17), and recellularize these with patient-derived CCA organoids (CCAOs) (n=3) to establish an *in vitro* model for studying the interaction between epithelial tumor cells and the microenvironment of the metastatic site. Decellularization resulted in acellular scaffolds with preserved ECM components. Local ECM heterogeneity was shown by the macro- and micro-scale mechanical properties as determined by rheology and micro-indentation. The CCAOs showed adherence and growth when combining them with the decellularized lung ECM (dLECM). The metabolic activity of CCAOs was diminished when cultured in dLECM compared to those cultured in BME, and was dictated both by the organoid line and the dLECM donor. Distinct CCAO gene expression profiles were observed between the two culture environments (BME and dLECM). This elucidates the effect of the culture environment on the behavior of CCAOs in an *in vitro* model. In conclusion, the convergence of CCAOs with their organ-specific location of metastasis obtained by decellularization, provides a valuable tool for integrating the ECM of the metastatic location in an *in vitro* model for the mechanistic study of cancer metastasis.

Keywords: decellularization, cholangiocarcinoma organoids, extracellular matrix, metastasis, recellularization.

Introduction

Bile duct cancer (cholangiocarcinoma, CCA) is a rare but highly aggressive subtype of primary liver cancer, with increased occurrence and mortality over the past few decades [1, 2]. The incidence rate of CCA ranges from 0.3-6 per 100.000 people annually in Western countries and over 6 per 100.000 in East Asia [3, 4, 5]. It usually affects the middle-aged and elderly, with a higher incidence in men compared to women, and rarely occurs before the age of 40 [6, 7, 8].

CCA includes three subtypes based on their anatomical location of origin: intrahepatic CCA (iCCA), perihilar CCA (pCCA) and distal CCA (dCCA). iCCA and pCCA are subtypes of primary liver cancer, and pCCA and dCCA are both extrahepatic CCA (eCCA) (Fig. 1) [1]. iCCAs arise from the intrahepatic biliary epithelium above the second-order bile duct and account for 10-20% of all CCAs. pCCA and dCCA arise from the extrahepatic biliary epithelium, with the cystic duct as the point of anatomical distinction, accounting for 50-60% and 20-30%, respectively [1]. The main growth patterns of iCCA, pCCA and dCCA are respectively mass-forming type (>90%), periductal infiltrating plus mass-forming type, and periductal infiltrating or intraductal-growing (Fig. 1) [5, 9].

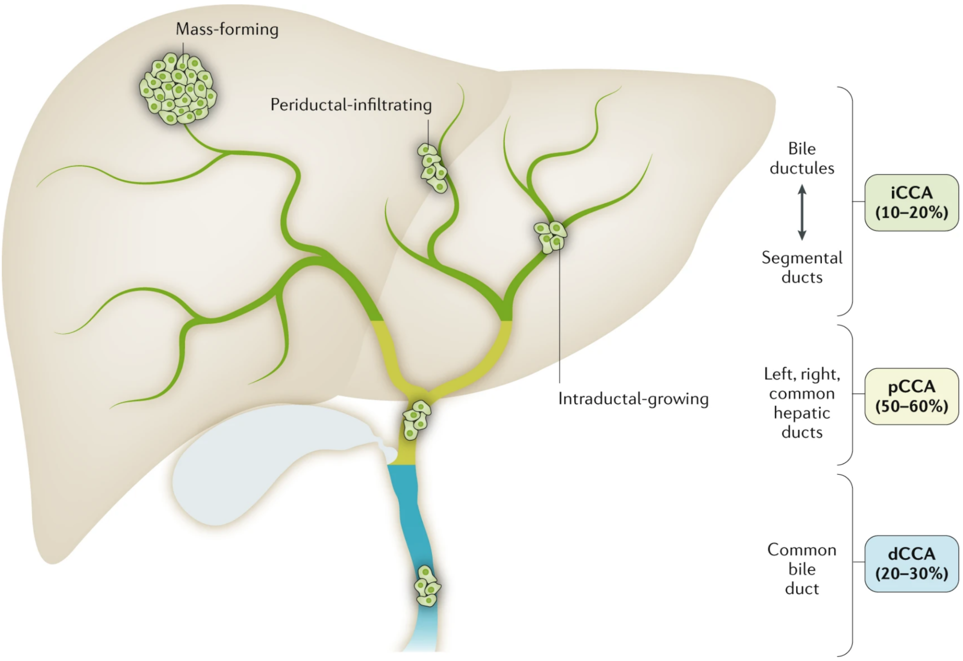

Figure 1: **Anatomical classification of CCA.** Locations of anatomic subtypes iCCA, pCCA and dCCA with their percentage of occurrence relative to all CCAs. Three main patterns of CCA growth are shown: mass-forming, periductal-infiltrating and intraductal-growing [1].

Established risk factors for the development of CCA include primary sclerosing cholangitis, choledochal cysts, hepatolithiasis, toxins, chronic hepatitis C virus-related and chronic hepatitis B virus-related liver diseases, liver cirrhosis and liver flukes [10, 11]. Additional less-well-established risk factors include diabetes, inflammatory bowel disease, human immunodeficiency virus, smoking, alcohol consumption and host genetic polymorphisms [11, 12]. Despite these risk factors, most CCA cases occur in individuals without evidence of chronic liver disease or other known risk factors [13, 14].

The 5-year survival rate amongst CCA patients is low, ranging from 7-20% [1]. This rate drops dramatically to 2% in distant metastasis cases [15]. The poor prognosis is attributed to the biological complexity of CCA, high intratumoral and interpatient heterogeneity, and late-stage diagnosis, often after the disease has already metastasized [16, 17, 18].

Current treatment options for CCA include surgical resection, liver transplantation, chemotherapeutics, intra-arterial treatments and local ablative therapies, depending on the CCA subtype and stage [19]. Surgical treatment is the

only potentially curative therapeutic option [19, 20]. However, approximately 60-88% of the patients are not eligible, including patients with distant metastasis [21]. Even after curative-intent surgery, a high recurrence rate (49-64%) and early local or distant metastases are experienced [19, 22].
The occurrence of distant metastasis in CCA is relatively common during the course of a patient's disease, ranging from 36.4-50.2% [23, 24, 25]. Lung and lymph nodes are frequently identified as preferred distant locations of metastasis [23, 24, 26]. Different metastatic locations have a distinct effect on the biological patterns of CCA and require different therapeutic strategies [27]. Lymph node metastases show better prognostic outcomes compared to lung metastases, but the cause is still unknown [26, 27]. Patients with metastasized CCA are unlikely to benefit from resection [28, 29]. If CCA is unresectable, patients may receive palliative care, including systemic chemotherapy [19]. Novel treatment options for metastasized CCA are urgently needed.

CCA, particularly iCCAs and pCCAs, are characterized by the deposition of abundant fibrotic or connective tissue, referred to as desmoplasia, and is associated with extracellular matrix (ECM) remodeling [30, 31]. The tumor microenvironment (TME) of solid CCA contains collagen-fibre-enriched ECM, cancer-associated fibroblasts, tumor-associated macrophages and innate immune cells, all interacting in a practical but complex way [19, 32]. This complex desmoplastic TME limits drug delivery and promotes CCA progression, including metastasis [33, 34]. Cancer-associated fibroblasts can modulate the epithelial-to-mesenchymal transition (EMT) of CCA cells, a process in which cells acquire migratory and invasive properties, leading to cell dissemination [35, 36]. Following the dissemination of cancer cells from the primary tumor, the cancer cells will undergo intravasation and survive in the lymphatic or blood circulation before extravasating and colonizing the metastatic organ (Fig. 2). The cancer cells are frequently in a state of dormancy, before switching to a state of proliferation and outgrowth which is dictated by the ECM and cell adhesion signaling [37, 38, 39]. However, mechanistic understanding behind the metastatic outgrowth of CCA and their micro-environmental cues remains lacking.

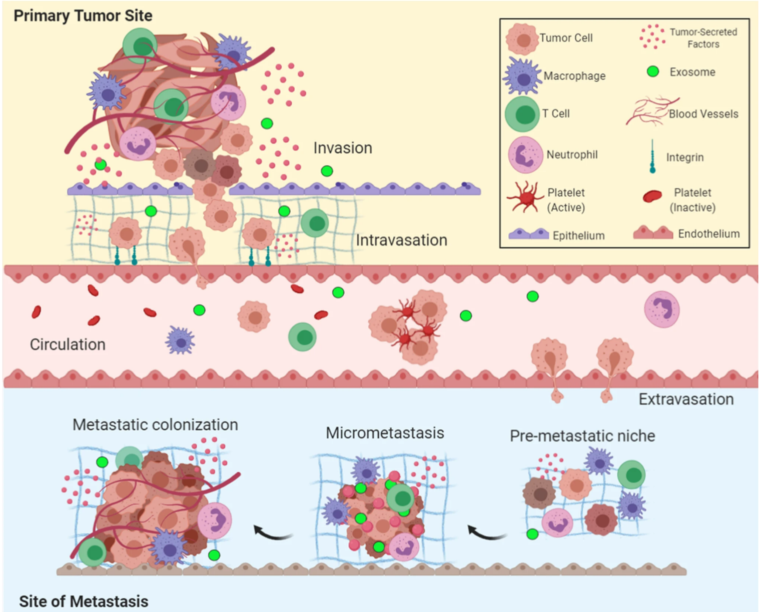

Figure 2: **Overview of the metastatic cascade.** The cascade includes five key steps: invasion, intravasation, circulation, extravasation, and colonization [40].

Effective CCA treatments are still lacking because current models do not recapitulate the micro-environmental cues, in which the ECM plays a key role [41, 42]. The ECM is a non-cellular physiologically active component responsible for cell-cell and cell-matrix interactions. Currently, to model and investigate CCA, immortalized CCA cell lines or patient-derived xenografts (PDX) are frequently employed, each with its advantages and disadvantages. Cell lines are able to expand rapidly and are frequently used for high-throughput drug screening. They have enabled groundbreaking advances in CCA cancer biology, such establishing the whole-genome sequence of distinct subtypes of CCA [43] and the association of specific metabolites with tumor cell metastasis and prognosis [44, 45]. However, cell lines do not mimic the cellular complexity, developmental biology, cell-cell and cell-ECM interactions of the *in vivo* tumor [18, 46]. PDX models are acquired by implanting patient's tumor tissue into immunodeficient mice. These models are physiological, frequently retain tumor histopathology and genetics, and contribute to the creation of accurate recapitulation of the original tumor morphology, with direct correlations to patient outcomes [47, 48, 49]. PDX models demonstrated their roles in developing new personalized anticancer drugs for CCA, identifying potential mechanisms of drug resistance, and testing therapeutics (lenvatinib, sorafenib [50]; crenigacestat [51]; anlotinib [52]; GNS561, cisplatin, gemcitabine [53]; L-asorbic acid [54]; NUC-1031 [55]; FGFR inhibitors [56]) [57]. However, the intrinsic limitations of PDXs include limited engraftment rates, long engraftment period (several months), labor-intensiveness, and compromised immune system, which complicates proper evaluation of tumor growth and patient response [49, 58]. Additionally, making these models is technically challenging, time-consuming and expensive, not to mention ethical issues.

CCA models recapitulating its metastasis are deficient, with the available options being limited to PDX models or other models utilizing animals, both of which have inherent limitations. For example, O'Dell et al. (2012) used mutant mouse strains (KRAS mutation and TP53 deletion), which resulted in local and distant iCCA metastasis [59]; Zhu et al. (2017) injected human CCA cell lines into mice to study lung metastasis [60], and Broutier et al. (2017) transplanted CCA organoids (CCAOs) derived from a patient with a history of metastasis in immunocompromised mice where lung metastases were found [61]. All of these models lacked a human-derived ECM of the organ of metastasis. Advancement in determining the impact of the host organ's specific characteristics on the behavior of disseminated cancer cells and their ability to colonize the organ, is impeded by a lack of models that accurately replicate the native structure of the organ.

Tumor-derived organoids, consisting of primary epithelial cells growing as 3D structures, have emerged in recent years as highly promising biological disease models due to their ability to self-renew and self-organize while retaining the physiological structure and mutational landscape of the original tumor [62, 63, 64]. They contribute to bridging the gap between cancer cell lines and complex xenografts. CCAOs have been successfully established and applied towards research on disease progression, the discovery of biomarkers, drug screening, and personalized medicine [61]. However, a current limitation of tumor organoid culture is the predominant use of Basement Membrane Extract (BME) or Matrigel as a culture environment that does not represent the native microenvironment, including its biomechanics, of the primary tumor or the metastatic niche [65, 66, 67]. The large variability in the batch-to-batch components of BME/Matrigel is an overall disadvantage of using it in cancer research, especially in the highly heterogeneous CCA [68, 69]. BME/Matrigel's limitations, including the absence of tissue-specific biochemical cues and ECM components, limited stability, costs and the need for mouse tumors, highlight the need for an alternative.

The relevance of the biomechanical and biochemical role of the ECM in cancer progression and tumor cell colonization has gained increased attention [39]. Cells sense and react to the mechanical properties of their environment, specifically the stiffness of the ECM [70, 71, 72]. Nonetheless, the interactions between CCA cells and the ECM of the metastatic organ remain not well comprehended. Decellularization, a technique that removes cells using enzymatic and chemical reagents while preserving the ECM, can be used to isolate the ECM of metastatic organs to study its composition and biomechanical properties [73, 74, 75]. Previous studies utilized decellularization to study tumor-ECM interactions: Tian et al. (2018) seeded colorectal cancer cells on lung and liver decellularized scaffolds to study organ-specific cancer metastases [76]; Sensi et al. (2020) decellularized colorectal cancer patient-derived scaffolds and recellularized these with adenocarcinoma cell lines [77]; Fecher et al. (2016) cultured human lung tumor cells on acellular rat lungs [78]; D'Angelo et al. (2020) seeded patient-derived decellularized ECM (dECM) scaffolds of tissue derived from the healthy colon, colorectal cancer, healthy liver and colorectal cancer liver metastases, with colorectal cancer cell lines. These studies indicate that decellularized scaffolds are frequently used as a biological model in combination with cancer cell lines rather than 3D structures such as organoids, limiting their applicability. But interestingly, van Tienderen et al. (2022) demonstrated that combining CCAOs with decellularized healthy liver and tumor liver scaffolds, could reveal how the ECM affects processes relevant to cancer such as proliferation, invasion and chemoresistance [79].

It is already known that the difference in treatment response between metastatic locations depends on the ECM and that niche-specific cell types and tissue structures have a significant role in metastatic progression [76, 80, 81]. For instance, Guarin et al. (2022) decellularized liver tissue to study the effects of the ECM on breast cancer cell proliferation and invasion, and showed that chemotherapy treatment alters the liver ECM to a pro-metastatic niche for cancer metastasis [82]. Nevertheless, modeling organ-specific metastatic colonization and recapitulating *in vivo* micro-environmental cues is a great challenge.

Elucidating the interactions between metastasized CCA and the ECM of the metastatic site, can be achieved by combining patient-derived CCAOs and organ-specific human-derived decellularized scaffolds of the metastatic locations.

In other words, recellularization of decellularized tissue with organoids. This way, limitations of utilizing BME/Matrigel, cell lines or animal models are surmounted. An improved patient-specific CCA metastasis model ultimately leads to discovering new drug targets, developing personalized treatments and reducing patient burden. Therefore, this study aims to decellularize and characterize human-derived lung and lymph nodes, and use the decellularized lung ECM (dLECM) in combination with patient-derived CCAOs to better model CCA metastatic colonization in lung and lymph nodes *in vitro*, to study metastatic cell-matrix interactions. For this, decellularization for lung and lymph nodes was optimized and confirmed, and dLECM and decellularized lymph node ECM (dNECM) were biochemically and biomechanically characterized. Additionally, growth patterns, metabolic activity, invasive patterns and gene expression profiles for CCAOs cultured in dLECM were evaluated and compared to CCAOs cultured in BME (Fig. 3).

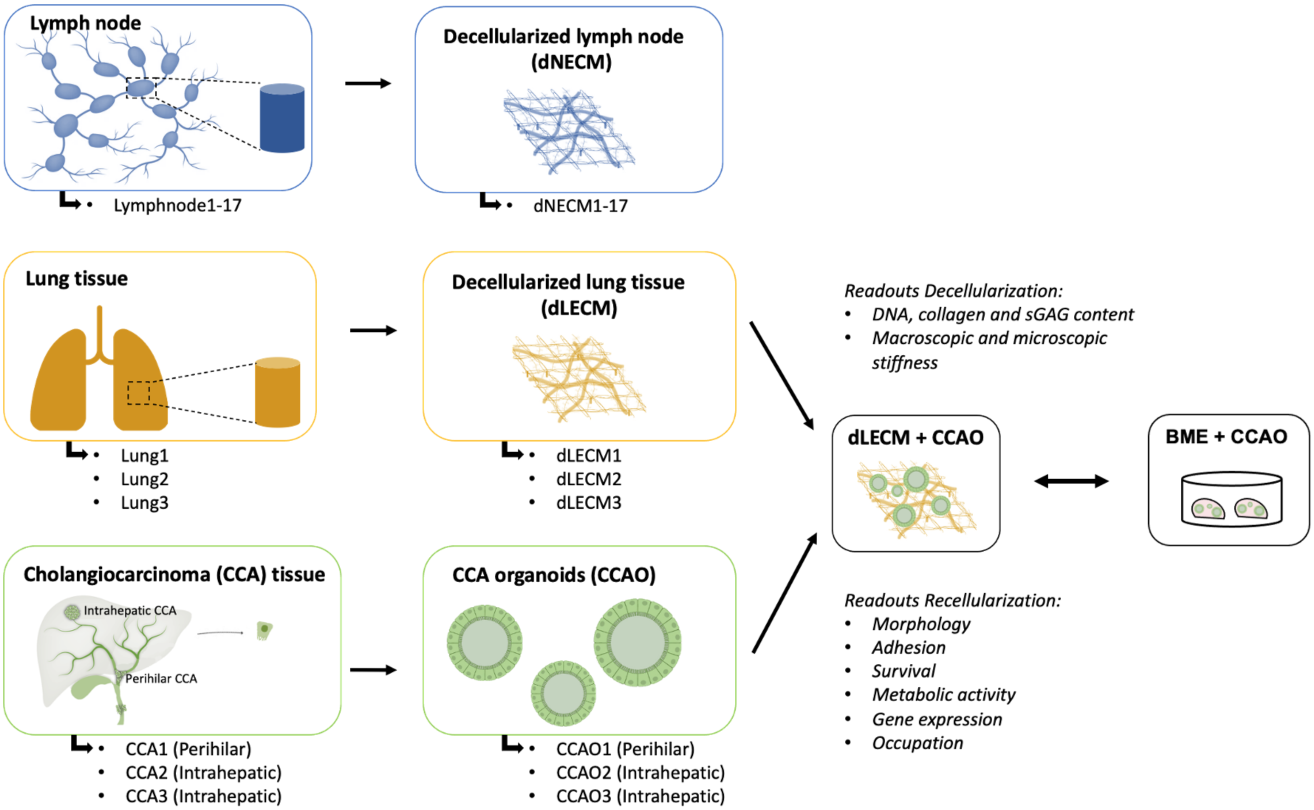

Figure 3: **Simplified schematic representation of the study.** Labels for the lung and lymph node donors and CCA patients utilized in the study are depicted.

Material and Methods

Sample procurement

Tissue collection

CCA tissue samples from three different patients (n=3, including n=1 pCCA and n=2 iCCA) were obtained from patients who underwent a curative-intent surgical resection, performed at the Erasmus MC in Rotterdam (Table 1 for patient information, Fig. 3). The Medical Ethical Council of the Erasmus MC approved the use of tissue for research purposes and patients provided written informed consent (MEC-2013-143). Samples were confirmed to be of tumor origin with histopathological assessment by a pathologist. CCA tissue samples were stored at 4°C in Belzer UW cold storage solution (UW, Bridge to Life) and, if used for organoid initiation, processed within 24 hours after collection. Lung tissue samples, measuring approximately 2x2x2 cm, were obtained from three different donors (n=3) whose lungs were rejected for lung transplantation for unknown reasons at Sahlgrenska University Hospital in Gothenburg, Sweden. The utilization of lung tissue was approved by the Swedish ethical review board in Lund (Dnr. 2008/413, 2011/581 and 2013/253). Lung tissue samples of peripheral lung were prepared by dissecting out cubes with a side length of approximately 10 mm with pleura remaining on one side and snap-freezing them in isopentane chilled with liquid nitrogen. Lymph nodes (n=17) were obtained from donors who donated their liver for a liver transplantation procedure, performed at the Erasmus MC in Rotterdam (MEC-2014-060). The utilized lymph nodes are hepatic hilar lymph nodes. Lung and lymph node samples were initially stored at -20°C and processed at a later stage for decellularization. Donor information for lung can be found in Table 1 and for lymph nodes in Table S2. Table S3 shows which lymph node was used per analysis. Labels for the samples used in this study are given in Figure 3 and the second column of Table 1.

Patient/Donor	**Sample label**	**Gender**	**Age**	**Localization tissue**	**Historical grade**	**Smoke history**
CCA patient 1	CCAO1	F	34	Perihilar	Moderate-well differentiated (grade 1-2)	-
CCA patient 2	CCAO2	M	60	Intrahepatic (segment 4)	Moderate-well differentiated (grade 1-2)	-
CCA patient 3	CCAO3	F	77	Intrahepatic (segment 4)	Poor-moderate differentiated (grade 2-3)	-
Lung donor 1	Lung1; decellularized: dLECM1	M	66	Peripheral	-	Former smoker (>10 years)
Lung donor 2	Lung2; decellularized: dLECM2	M	68	Peripheral	-	Never smoked
Lung donor 3	Lung3; decellularized: dLECM3	M	66	Peripheral	-	Current smoker
Lymph node donor 1-17	Lymph node1-17; decellularized: dNECM1-17	-	-	Hepatic hilar region	-	-

Table 1: **CCA patient, lung donor and lymph node donor information and characteristics.**

Initiation and propagation of patient-derived cholangiocarcinoma organoids

Initiation of CCAOs was done as previously described [61]. Organoids were passaged in a 1:3-1:6 ratio approximately every 7 days, depending on their proliferation rate. Expansion medium (EM, Table S1) was refreshed every 3 or 4 days. Organoid cultures between passage number 145-180 were used. Passaging started with taking off the EM and collecting the organoids in a 15 ml tube by adding ice-cold Advanced Dulbecco's Modified Eagle Medium/F12 (AdvDMEM, Gibco) supplemented with 1% penicillin-streptomycin, 1% HEPES, 1% ultraglutamine, 0.2% primocin to the wells and scraping/pipetting. Subsequently, ± 8 ml ice-cold AdvDMEM was added to the 15 ml tubes. After centrifugation (5000rpm, 5 minutes, 4°C), the supernatant was removed and the pellet was re-suspended in ice-cold AdvDMEM while mechanically breaking the organoids by pipetting up and down. After another centrifugation step (5000rpm, 5 minutes, 4°C), the supernatant was removed and the cell pellet was re-suspended in BME (Cultrex). The mixture of cells and BME was plated in droplets of 25 μl in 12-, 24- or 48-well suspension culture plates (Greiner or Sarstedt) (Fig. S1). After upside-down incubation at 37°C for 30 minutes, EM was added (250 μl per well in a 48-well plate) to the culture plates and returned to the 37°C incubator.

Decellularization

Decellularization procedure of human lung tissue and lymph nodes

Lung tissues were embedded in tissue-tek optical cutting temperature compound, mounted on a metal holder and cut with a cryotome (Leica) at -15°C into 400 μm thick slices (Fig. 4B2). 400 μm thick lung slices and entire lymph nodes were placed in a flask on a multi-position magnetic stirrer (Fig. 4B5, S2A). Lymph nodes were not cut into smaller slices before decellularization because of their relatively small surface area and otherwise disintegration of the lymph nodes during decellularization. An identical decellularization protocol was used for both tissue types. The protocol was based on the one described by van Tienderen et al. (2023) for liver and liver biopsy samples to minimize the effect on recellularization by the decellularization method [83]. This decellularization protocol was modified by adding an overnight washing step of approximately 16 hours with TX-100. First, tissue samples were washed for 30 minutes with dH_20, 1 hour with 9% hypertonic saline (NaCl) and again for 30 minutes with dH_20 to remove traces of blood, debris and tissue-tek optical cutting temperature compound by using osmotic effect. After that, all tissue samples were decellularized with a solution consisting of 4% Triton X-100 and 1% NH_3 (hereafter referred to as TX-100 solution). TX-100 solution was replaced every hour for 10 cycles, including two overnight (O/N) cycles of approximately 16 hours, which resulted in transparent tissues (Fig. 4B6). Subsequently, the tissues were washed with Phosphate-buffered saline (PBS; Gibco, HyClone) for 1 hour to remove traces of TX-100. Subsequently, tissues were incubated with DNase solution (2 mg/l DNase type 1 (Sigma) in 0.9% NaCl + 100 mM $CaCl_2$ + 100 mM $MgCl_2$) for 3.5 hours at 37°C on the magnetic stirrer. Finally, tissues were washed two times with PBS (Table 2). Biopsy samples were taken before and after decellularization for various analyses. dNECMs and dLECMs of 400 μm were collected in 50 ml tubes and kept frozen in PBS at -20°C until further use.

Solution	**Time**
H_2O	30 minutes
Hypertonic saline (9% NaCl)	1 hour
H_2O	30 minutes
4% Triton X-100 + 1% Ammonia*	1 hour
Previous step 9x including 2x O/N	1 hour 7x, O/N 2x
PBS 1x	30 minutes
DNase at 37°C	3.5 hour
PBS 1x	30 minutes 2x

Table 2: **Decellularization protocol used.***= Repetition of this cycle at least 2 times before first O/N step.

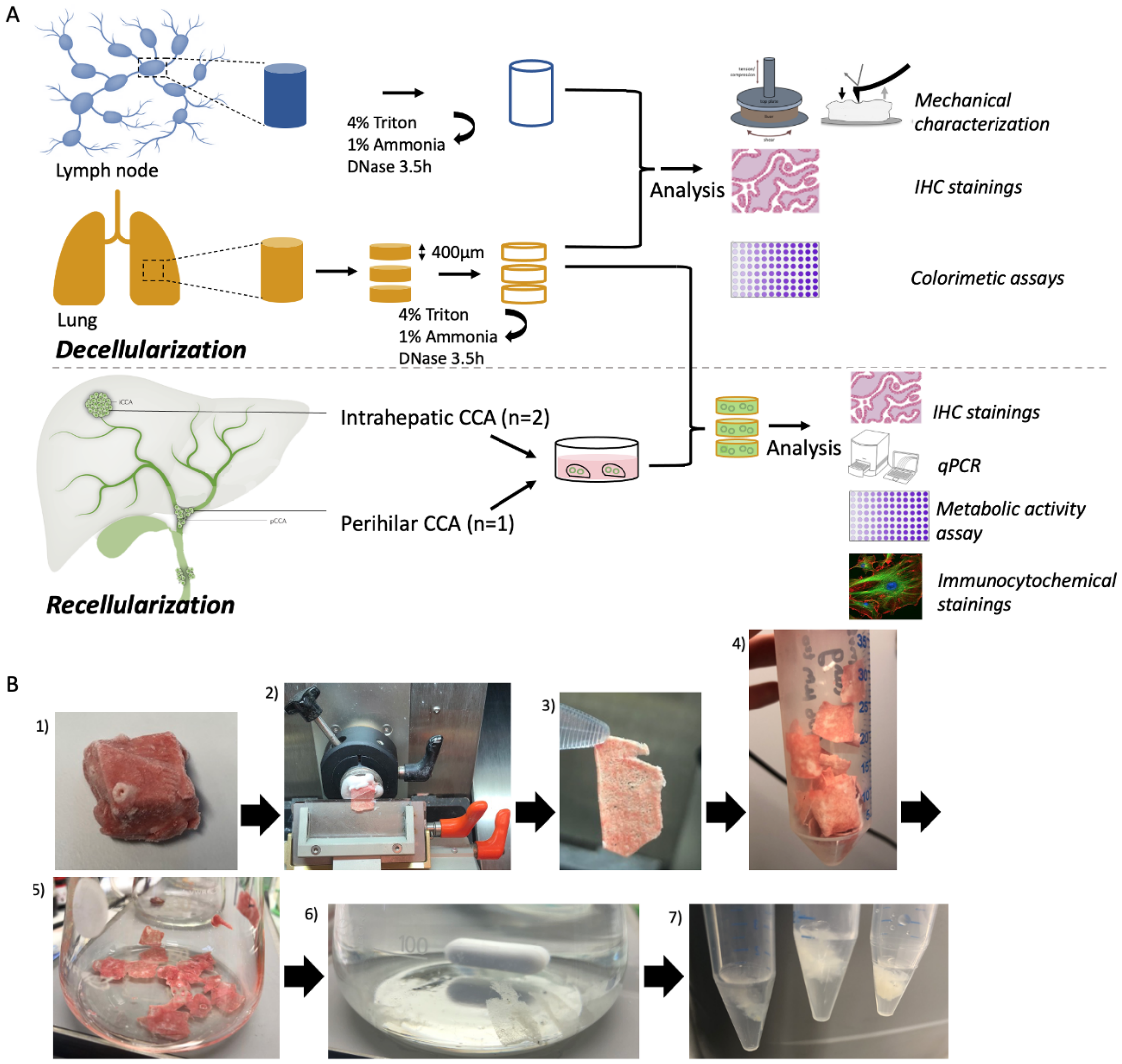

Figure 4: **Decellularization procedure of human lung and lymph nodes, and recellularization procedure of dLECM with CCAOs. A)** Schematic representation of the decellularization (top) and recellularization (bottom) procedure and subsequent analysis. **B)** Overview of sequential steps to decellularize lung tissue: **1)** lung tissue, **2)** cutting process using a crytome, **3,4)** collecting 400μm slices lung, **5,6)** experimental set-up for decellularization steps (Table 2) on a magnetic stirrer and **7)** resultant dLECM.

Confirmation of decellularization procedure

Biopsies and decellularized tissue were fixed in 4% paraformaldehyde (PFA; Fresenius Kabi), solidified in 2% agarose in PBS, embedded in paraffin and sectioned at 4 μm using a microtome (HM 325) (Fig. S3). Slides of samples before and after decellularization were stained with either hematoxylin and eosin (H&E), 4',6-diamidino-2-phenylindole (DAPI; Vectashield, Vectorlabs) or picrosirius red (PSR; Sigma) according to standard staining procedures. Collagen type 1 and collagen type 3 are stained according to standard protocol by the pathology department (ErasmusMC, The Netherlands). Slides were imaged with a Zeiss Axioskop 20 microscope and captured with the Zeiss Axiocam 305 color or imaged and captured with Nanozoomer 2.0-HT (Hamamatsu). DAPI-stained slides were analyzed using an EVOS microscope (Thermo Fisher Scientific). Additionally, deoxyribonucleic acid (DNA) was isolated from lung and lymph nodes, before (T=0) and after (T=decell) decellularization, using the QIAamp DNA Micro Kit (Qiagen) according to the manufacturer's protocol. Subsequently, the total DNA content was measured using a Nanodrop spectrophotometer (Thermo Fisher Scientific; lung n=3, lymph node n=15) and corrected for the corresponding wet weight of the measured sample (ng DNA/mg wet tissue). The wet weight of the samples was weighed before performing the analysis.

Collagen and sulfated glycosaminoglycan quantification

The total collagen content of lung and lymph nodes before (T=0) and after (T=decell) decellularization (lung n=3; lymph node n=4) was determined using a Total Collagen Kit (Quickzyme Biosciences; according to manufacturer's protocol. The absorbance of the collagen-binding dye was measured in a transparent 96-well plate at 570 nm using an infinite M nano plate reader (Tecan). Background absorbance was subtracted. The content was corrected for the wet-weight of the corresponding samples (μg collagen/mg wet weight tissue).
Sulfated glycosaminoglycan (sGAG) content of lung and lymph nodes before (T=0) and after (T=decell) decellularization (lung n=3, lymph nodes n=5) was determined using a Blyscan Sulfated Glycosaminoglycan Assay (Biocolor) according to the manufacturer's protocol. Samples were digested in a Papain (Sigma) solution (10 mg/ml) at 65 °C for 3 hours. The absorbance was measured in a transparent 96-well plate at 656 nm using an infinite M nano plate reader (Tecan). The wet-weight of the samples was weighed before performing the analysis.

Nanoindentation measurements and analysis

The effective Young's modulus (E) of decellularized tissue samples was measured using a Chiaro Nanoindenter (Optics11 Life) (Fig. S2B). dLECM (n=3) and dNECM (n=3) were glued inside a 35 mm petri dish using NOA61 or NOA81 (Norland) and a UV torch (Walther Pro). The sample and probe were immersed in PBS before the measurement started. The stiffness of the probes used for dLECM and dNECM was respectively 0.027 N/m and 0.030 N/m. The probes had a tip radius of 3 μm and were ball-shaped. First, the sample was indented to a depth of 2 μm in 4 seconds (0.5 μm/s). Then, the indentation was held at 2 μm depth for 1 second and finally the probe was retracted in 1 second. At least one matrix scan of 3x3 with a distance of 5 μm between indentation points was performed per dECM. The Hertzian contact model in the Optics 11 data viewer software (version V3.4.7) was used to calculate the effective Young's modulus [84]. Measurements with an unreliable model fit ($R^2<0.9$) were considered as outliers and disregarded from further analysis.

Rheology measurements and analysis

A rotational rheometer (KINEXUS PRO; Technex) with a flat parallel plate geometry with a diameter of 20 mm was used to determine the Young's modulus of the decellularized tissues (Fig. S2C). All measurements were performed at 37°C and obtained by the rSpace software. dLECM (n=3, 400 μm thick) and dNECM (n=3) were placed on the bottom plate. Next, the top plate was lowered to a gap height of 2 mm (dLECM1, dLECM2), 3 mm (dLECM3, dNECM16) or 1.8 mm (dNECM2, dNECM10). First, the surface contact point was found by decreasing the gap at a rate of 0.01 mm/s with a measurement of the normal force every 0.01 second, which the software used to automatically determine the contact point. Subsequently, a shear oscillation frequency sweep (f: 10-0.01 Hz, slope: 10 points per decade) was performed to determine the viscoelastic properties of the samples. Subsequently, the dECM was compressed $4*10^{-4}$ mm every second for 13.3 minutes. Then, another shear oscillation frequency sweep (f: 10-0.01 Hz, slope: 10 points per decade) was performed. An approximation of the Young's modulus (E) was determined over the whole range of compression. The strain was calculated by ($h-h_0/h_0$) where h is the gap while measuring and h_0 is the initial gap when the surface contact point was found. The stress was calculated by (strain+1)*(Normal force/initial area) where the initial area was calculated by π*(sample radius)^2, following the Cauchy stress calculations [85]. In this way, the data were corrected for the size of each sample and increase in size after each compression step. The gradient slope over the whole range of compression resulted in an approximation of the Young's modulus.

Recellularization

Preparation of decellularized lung scaffolds for organoid culture

One day before recellularization, scaffolds were washed with sterile PBS three times, followed by washing with AdvDMEM three times. Subsequently, the scaffolds were incubated overnight at 37°C with AdvDMEM, supplemented with 10x the concentration of penicillin- streptomycin, primocin and antiobiotic-antimycotic (Gibco) to avoid infections in the recellularization experiments. dLECMs were washed three times with AdvDMEM on the day of recellularization. The washed scaffolds were placed in the middle of a new 12- or 24-suspension or culture well plate (Greiner or Sarstedt) and were folded out as much as possible using a needle or tweezer.

Recellularization procedure

CCAOs (n=3) grown in BME (Cultrex) droplets were harvested by removing the BME droplets from the wells using ice-cold AdvDMEM as previously described. After removal of BME and AdvDMEM from the cell pellet, 1 ml trypsin (TrypLE, Thermo Fisher Scientific) was added. The suspension was incubated at 37°C for 15 minutes while applying mechanical disruption with a pipette every 5 minutes until organoid fragments were dissociated into small aggregates and single cells. Subsequently, 10 μl of the suspension was added to 10 μl Trypan Blue (Thermo Fisher Scientific) for cell count using disposable cell counting chambers (Kova). After 15 minutes of incubation, trypsin was directly inactivated by adding cold AdvDMEM. The suspension was centrifuged for 5 minutes (1500rpm, 4°C) and the resulting cell pellet was re-suspended in EM to obtain the total amount of cells needed (approx. 200.000 cells/scaffold). Per dLECM, Cells in EM (5 μl) were added on top of the unfolded scaffolds in a 12- or 24-suspension or culture well plate (Greiner or Sarstedt) (Fig. S4). The recellularized scaffolds were incubated for 3 hours at 37°C before adding 350-500 μl EM to the recellularized scaffolds. EM was refreshed every 3 or 4 days. Organoid cultures in BME were used as a control. After 18 days, experiments were terminated. During these 18 days, 3-4 recellularized scaffolds per replicate were used for metabolic activity assessment. At day 18, the recellularized scaffolds were added to 700 μl QIAzol lysis reagent (Qiagen) and stored at -80°C for quantitative polymerase chain reaction (qPCR) analysis. The remaining recellularized scaffolds were fixed in 4% PFA at 4°C for 25 minutes. Subsequently, PFA was replaced by PBS and stored at 4°C until further use. These samples were used for histological analysis or whole-mount staining.
Recellularization was also performed with dNECM. Preliminary results are depicted in the supplementary results section (Figure S14).

RNA isolation, cDNA synthesis and RT-qPCR

For ribonucleic acid (RNA) isolation, QIAzol lyzed samples (3-4 recellularized scaffolds per CCAO+dLECM replicate or CCAOs cultured in BME) were homogenized with a TissueRuptor (Qiagen). Messenger RNA was isolated with a miRNeasy kit (Qiagen) according to the manufacturer's protocol. A Nanodrop spectrophotometer (Thermo Fisher Scientific) was used to measure RNA content. 500 ng complementary DNA was made by adding 5x PrimeScript RT Master Mix and dH_2O to isolated RNA and inserted into a 2720 Thermal Cycler (Applied Biosystems) or SimpliAmp Thermal Cycler (Applied Biosystems). qPCR was performed according to standard procedures with 10 μl SYBR select master mix, 1 μl primers, 4 μl dH_2O and 5 μl complementary DNA per reaction. All the tested primer sets are listed in Table S4. The housekeeping genes Glyceraldehyde-3-Phosphate Dehydrogenase (GAPDH) and Hypoxanthine-guanine-fosforibosyl-transferase (HPRT) were used as reference genes. The geometric mean of the two housekeeping genes was used for determining the ΔCt and ΔΔCt values of the genes as described in Vandesompele et al. 2002 [86]. Fold changes ($2^{-\Delta\Delta Ct}$) of selected genes of recellularized scaffolds were calculated compared to matched CCAOs grown in BME.

Live/Dead staining

CCAOs cultured in dLECM for 15 days were incubated in EM supplemented with 100 μg/ml Hoechst (Hoechst 33342, Thermo Fisher Scientific), 50 μg/ml propidium iodide (PI, Sigma-Aldrich) and 0.5 μM calcein (Calcein-AM, Thermo Fisher Scientific) at 37°C for 30 minutes protected from light. Images were made with an EVOS FL fluorescent microscope (Thermo Fisher Scientific).

Immunofluorescent staining

On day 18 of recellularization, the recellularized dLECMs were fixated in 4% PFA for 25 minutes and washed with PBS three times. Subsequently, samples were permeabilized with 0.1% TX-100 in PBS for 30 minutes and again washed with PBS three times. After that, samples were exposed to 5% blocking epitope Bovine Serum Albumin (BSA) in PBS for 1 hour. Vimentin (1:100, Bio-connect) was added to the samples and incubated overnight at 4°C. After washing with PBS five times, the samples were incubated with secondary antibody Alexa Fluor™488 (1:200, Thermo Fisher Scientific) for 1 hour at room temperature. Antibody Phalloidin Alexa Fluor™488 (1:200, Thermo

Fisher Scientific) for cytoskeletal staining was incubated for 1 hour and nuclear staining with DAPI was incubated for 30 minutes at room temperature before confocal imaging.

Confocal immunofluorescence imaging

Recellularized dLECMs were imaged using a Leica 20x (NA 1.0) water dipping lens on a Leica TCS SP5 II confocal system. Fiji/ImageJ software was utilized to post-process the images.

Histological staining

PFA-fixed samples were solidified in 2% agarose in PBS. They were embedded in paraffin and sectioned at 4 μm using a microtome (HM325). Decellularized and recellularized scaffold slides were stained with H&E according to a standard protocol.

Cell metabolic activity assessment

PrestoBlue™ Cell Viability Reagent (Thermo Fisher Scientific) was used to assess metabolic activity of CCAOs in dLECM and in BME for the same sample at day 1, 4, 8, 11, 14, 18 after recellularization. At day 1, the recellularized scaffolds were placed in a new 24-well plate. Presto Blue compound was diluted 10-fold (1:10) in EM, filtered and pre-warmed in a 37°C waterbath for 10 minutes. EM was removed from the recellularized scaffolds and the CCAO cultures in BME, and 500 μl Presto Blue solution was added to each well. These culture plates were incubated at 37°C for 3.5 hours protected from light. Subsequently, the medium was plated in a 96-well plate in triplicate. The absorbance was measured using an CytoFluor Multi-Well plate Reader series 4000 (Perseptive Biosystems) with excitation of 530nm and emission of 590nm. Background absorbance was measured using non-recellularized dLECM (n=3) and empty BME domes. Background measurements were subtracted and data were normalized to day 1. Significant differences between metabolic activity of recellularized combinations were determined for separate time points (Two-Way ANOVA multiple comparison test) as for the entire culture period of 18 days (Two-Way ANOVA matched by time).

Statistical analysis

Statistical analyses were performed using GraphPad Prism (version 8, GraphPad Software). Graphs were plotted with their mean and standard deviation (SD). Paired t-test was used to determine significance in DNA content. Two-way ANOVA test was performed for multivariate analysis with multiple comparison testing for different time points or different donors (i.e., the sGAG/collagen contents, metabolic activity). Mann-Whitney U test was performed for determining significance in the mechanical properties. In all tests, a p-value of <0.05 was considered significant.

Results

Decellularization of lung tissue and lymph node results in acellular ECM scaffolds

First, lung and hepatic hilar lymph nodes were decellularized. Histological evaluation and DNA content quantification revealed successful decellularization (Fig. 5). H&E staining demonstrated that nuclear material and cellular debris were removed while the ECM was preserved after decellularization for both lung and lymph node (Fig. 5A, S5A,B). Lung sections show hollow structures of the alveoli and bronchiole before and after decellularization (Fig. 5A, S7) [87]. Lymph node sections show their typical reticular meshwork architecture in T=0 conditions (Fig. 5A, S5A,B) [88]. DAPI staining confirmed the removal of nuclear material from lung and lymph node (Fig. 5B, S5C). Similar to other decellularized organs, lung and lymph nodes appeared translucent white after decellularization (Fig. 5C) [76, 83, 89, 90]. Nuclear material loss was confirmed by DNA quantification. Figure 5D showed a significantly decreased DNA content for lung ($p=0.003$) and lymph nodes ($p=0.0004$) after decellularization. The average DNA concentration before decellularization was for lung 250.2 ng DNA/mg wet tissue ($n=6$, consisting of 3 donors measured in biological replicate, $SD=98.7$ ng) and for lymph node 720 ng DNA/mg wet tissue ($n=15$, $SD=569.8$ ng), indicating a higher cell density compared to lung. After decellularization, the DNA content was 23.3 ng DNA/mg wet tissue ($n=6$, $SD=11.2$ ng) for dLECM and 19.9 ng DNA/mg wet tissue ($n=15$, $SD=17.6$ ng) for dNECM, equaling a reduction of 90.7% for lung and 97.2% for lymph node. Both absolute values and percentage reduction (i.e., <50 ng DNA/mg wet tissue and 90% reduction in DNA content) adhere to common criteria for complete cell removal [91, 92]. However, the requirement to obtain <50 ng DNA/mg wet tissue after decellularization was not met for 2 out of 15 lymph nodes. These 2 lymph nodes were not included for further analysis.

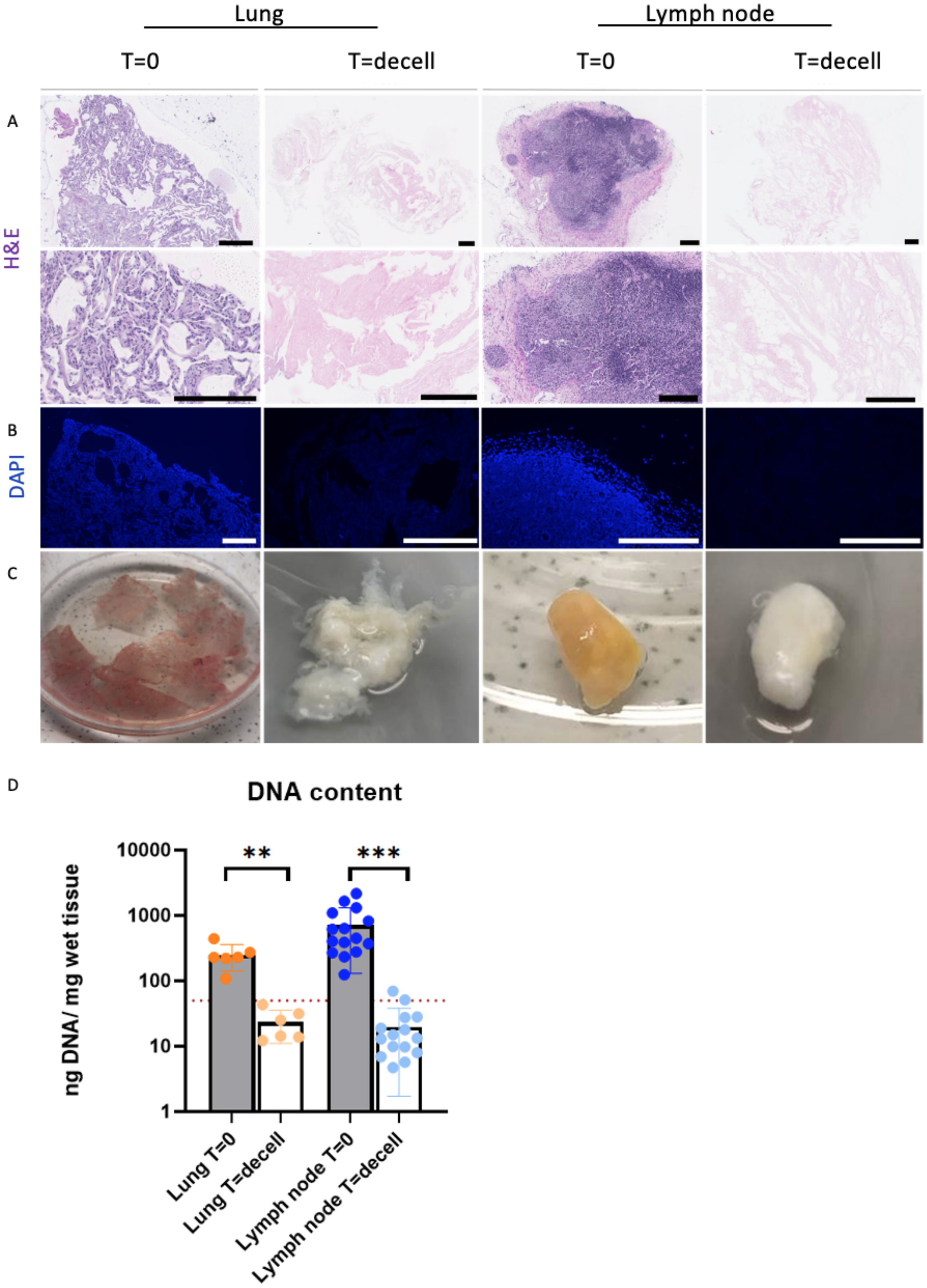

Figure 5: **Acellular ECM scaffolds of lung and lymph nodes obtained by decellularization. A)** Representative H&E stainings of lung and lymph node before (T=0) and after (T=decell) decellularization show efficient removal of cells from the scaffold and maintenance of ECM structure. Scale bars indicate 250 μm. **B)** Representative DAPI stainings of lung and lymph node before and after decellularization confirmed the removal of nuclear material from the scaffold. Scale bars indicate 400 μm. **C)** Lung slices of 400 μm thick and an entire lymph node of 0.75 cm thick before and after decellularization show the transformation in color from brown/yellow to translucent white. **D)** Quantitative DNA content analysis of lung (n=6, consisting of 3 donors measured in biological replicate, p=0.003) and lymph node (n=15, p=0.0004) before and after decellularization shows a significant decrease in DNA content, confirming successful decellularization. Error bars indicate ± SD. The red dotted line indicates the threshold of 50 ng DNA/mg wet tissue, a common criterion for adequate cell removal [91]. Two lymph nodes did not meet the requirement of <50 ng DNA/mg wet tissue and were not used in further analysis. Thus, utilizing the same decellularization method for lung and lymph node resulted in successful decellularized tissue.

Decellularized lung and lymph node scaffolds retain ECM components

To further characterize the dLECM and dNECM, the level of preserved ECM-related components was assessed (Fig. 6). PSR staining revealed retention of a relative high presence of collagen, the primary structural component of the ECM, in dLECM and dNECM, indicating an intact ECM architecture (Figure 6A). Quantitative analysis of collagen shows similar results. The collagen content significantly increased after decellularization for both lung (before decellularization: 3.36 μg/mg wet tissue, SD=0.54 μg/mg; after decellularization: 31.49 μg/mg wet tissue, SD=5.94 μg/mg) and lymph node (before decellularization 1.53 μg/mg wet tissue, SD=0.58 μg/mg; after decellularization: 43.46 μg/mg wet tissue, SD=15.63 μg/mg) (Fig. 6B). This represents a 9.4-fold and 28-fold increase for lung and lymph node respectively. The apparent increase in collagen content is mainly due to the cell removal and thus weight, whereas the absolute collagen content remains retained.

Lung and lymph nodes were stained for collagen type 1 and 3 before and after decellularization to determine which collagen types were preserved (Fig. 6C, D). In the lung, fibrillar collagen type 1 and 3 predominate in the alveolar wall and alveolar septa, primarily contributing to lung mechanics and architecture [93, 94, 95]. Collagen type 1 is stiffer and confers tensile properties, while collagen type 3 permits multidirectional flexibility [96, 97]. The main components of lymph nodes are collagen types 1 and 3, which are also components of reticular fibers [98, 99]. Figures 6C, 6D and S6 demonstrate diffuse expression and retention of collagen type 1 and type 3 after decellularization for both lung and lymph nodes. Collagen predominates on the edges of lymph nodes, while the lung exhibits an overall positive collagen staining pattern with cells interspersed throughout before decellularization.

Sulfated glycosaminoglycans (sGAGs) are critical in regulating several cancer-related processes, such as angiogenesis, invasion, proliferation, and metastasis [100, 101]. sGAGs were preserved after decellularization for both lung and lymph nodes. The sGAG content decreased for both lung (before decellularization: 11.63 μg/mg wet tissue, SD=2.32 μg/mg; after decellularization: 8.49 μg/mg wet tissue, SD=1.94 μg/mg) and lymph node (before decellularization: 11.65 μg/mg wet tissue, SD=2.82 μg/mg; after decellularization 6.20 μg/mg wet tissue, SD=2.54 μg/mg). The sGAG content slightly decreased with a 1.4-fold for lung and 1.9-fold for lymph nodes. The minor variation between lung and lymph nodes may be attributed to the higher cell density in lymph nodes, resulting in a relatively higher loss of intracellular sGAGs during decellularization. Overall, decellularization of lung and lymph nodes resulted in preserved components of the ECM.

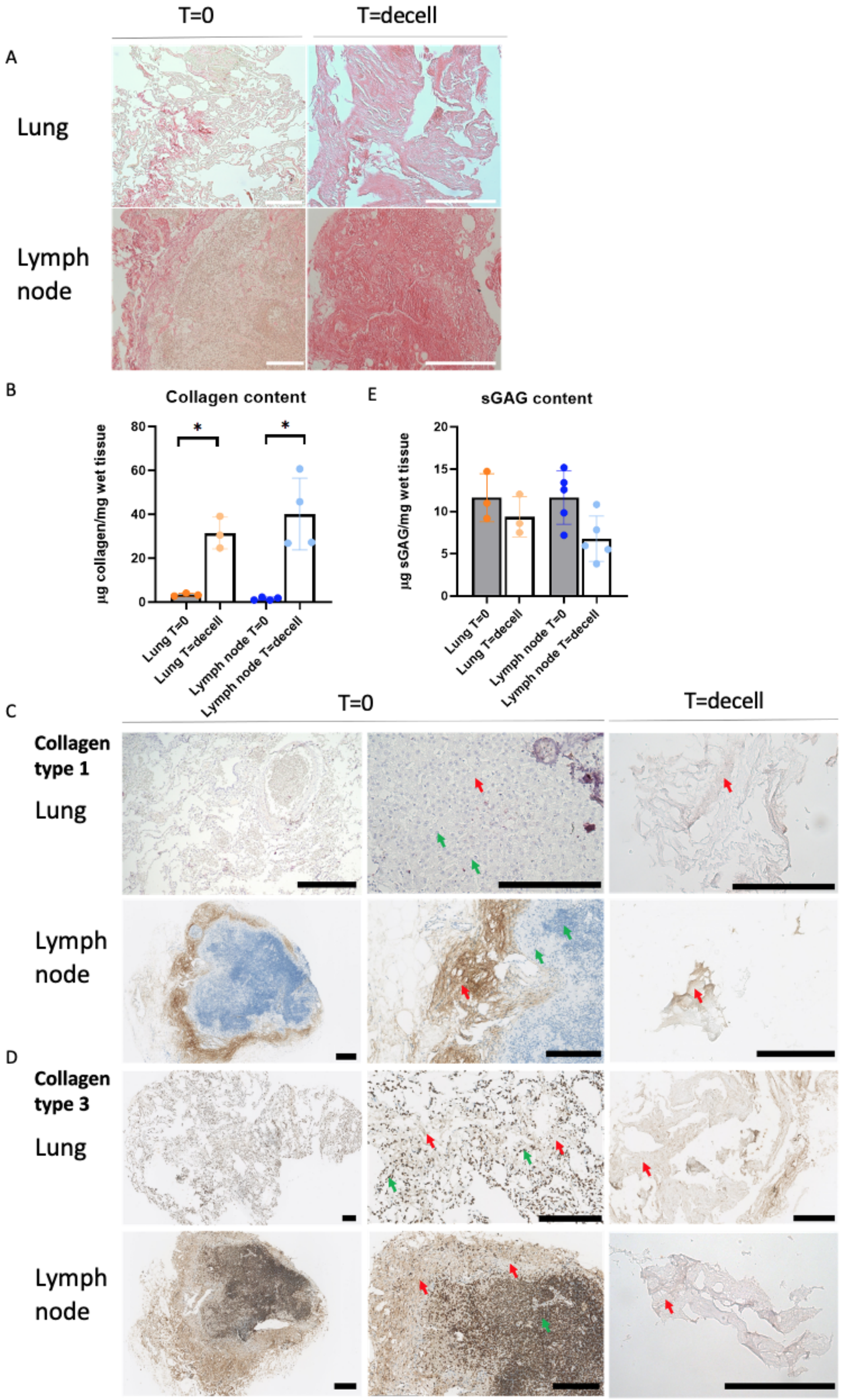

Figure 6: **Preservation of ECM proteins for lung and lymph node after decellularization. A**) PSR staining of lung and lymph node before (T=0) and after (T=decell) decellularization shows retention of collagen and intact ECM architecture. Scale bars indicate 200 μm. **B)** Quantitative collagen content analysis of lung (n=3, p=0.02) and lymph node (n=4, p=0.02) before and after decellularization showing retention of collagen. **C,D)** Collagen type 1 (C) and collagen type 3 (D) staining of lung and lymph node before and after decellularization which demonstrates the presence of collagen type 1 and collagen type 3 in dLECM and dNECM after decellularization. Red arrows indicate ECM, green arrows indicate cells. Scale bars indicate 250 μm. **E)** Quantitative sGAG content analysis of lung (n=3, p=0.5) and lymph node (n=5, p=0.07) before and after decellularization showing retention of sGAG.

Variation in mechanical properties of decellularized lung and lymph node scaffolds

Tissue functioning relies on the three-dimensional network formed by collagens, which is central to providing the mechanical properties through its architecture [102]. To provide novel information about the macro- and microscopic mechanical properties of dLECM and dNECM, rheology measurements and nanoindentation were performed, respectively. Macroscopic properties of dLECM and dNECM were determined by assessing rheological properties under compression. The approximation of the Young's modulus (E), determined over the whole range of compression, was 0.46 kPa (SD=0.18) for dLECM and 0.53 kPa (SD=0.41) for dNECM (Fig. 7A). dNECMs show more heterogeneity in the macro-scale stiffness in comparison to dLECMs. At a microscopic level, the effective Young's modulus was obtained by nanoindentation and ranged from 0.15-52.3 kPa for dLECM and 0.05-40.9 kPa for dNECM (Fig. 7B). The effective Young's modulus did not make any assumptions regarding Poisson's ratio, in contrast to the Young's modulus. No significant differences were observed between the different donors' micro-scale stiffness for both dLECM as dNECM. The large standard deviation in the micro-scale stiffness for both tissue types indicates heterogeneity (Fig. 7B). Heatmaps of the nanoindentation measurements confirm the intra-sample heterogeneity for both dLECM and dNECM (Fig. 7B,C).

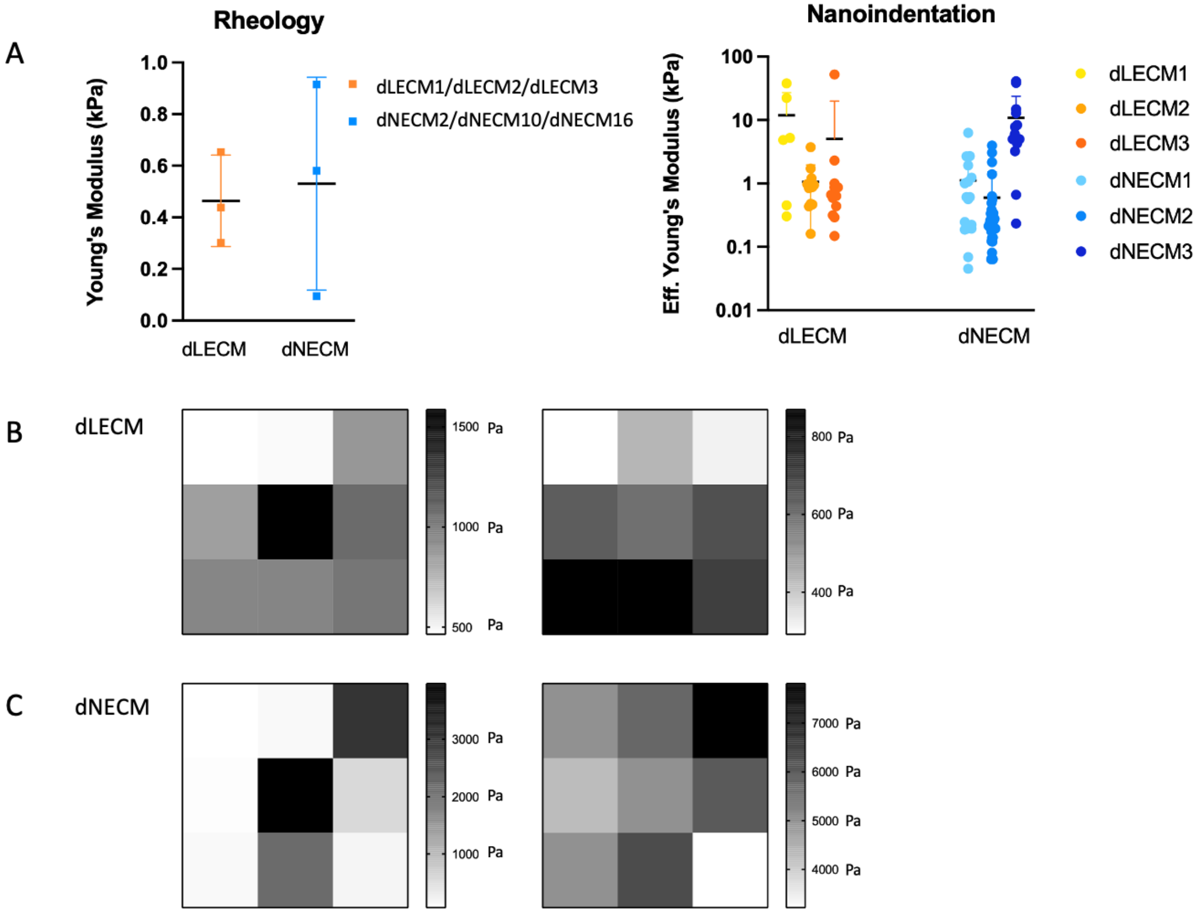

Figure 7: **Macroscopic and microscopic mechanical characterization of dLECM and dNECM. A)** Left: Rheological measurements showing the Young's Modulus of dLECM (n=3) and dNECM (n=3). More heterogeneity in macro-scale stiffness is seen in dNECM. Right: Effective Young's Modulus measured by nanoindentation (3x3 matrix scans) for dLECM (n=3) and dNECM (n=3) demonstrate heterogeneity in the micro-scale stiffness. Micro-scale stiffness ranges from 0.15-52.3 kPa for dLECM and 0.05-40.9 kPa for dNECM. **B,C)** Representative heatmap of a 3x3 matrix scan with 5μm between nanoindentations and a total measured area of 15x15 μm per dECM. B) dLECM nanoindentations (left: dLECM2, right: dLECM3) and C) dNECM nanoindentations (left: dNECM3, right: dNECM2).

Decellularized lung scaffolds support the culture of patient-derived CCAOs

Patient-derived CCAOs (n=3) were cultured in BME, harvested and seeded on dLECM (n=3) to mimic metastatic outgrowth in the lung and to assess the effect of the decellularized scaffold on the cell response. CCAOs grown in BME were spherical in shape and proliferated similarly as previously described (Figure 8A, S10) [61, 103]. The biocompatibility of dLECM was extensively assessed by culturing CCAOs in dLECM for 18 days (Fig. 8). Bright field microscopy images showed the adhesion of single cells and cellular clumps of CCAOs to the dLECM at day 1 after recellularization (Fig. 8B, S11). The organoids in dLECM had similar morphology to BME-cultured organoids at day 7 (Fig. 8A, B, S10), and eventually transformed into a transparent rim composed of organoids surrounding the edge of the dLECM at day 14 (Fig. 8B, S11). Bright field images only provided a first indication of cell proliferation since the thick density of the ECM limited in-depth evaluation.

The recellularized dLECM mainly contained alive cells as assessed by live/dead staining with Calcein-AM and propidium iodide (Fig. 8C, S13). Green organoid structures are visibly distributed on the scaffold, indicating the viability of organoids dispersed throughout the dLECM, similar to standard culture conditions in BME (Fig. S10).

Specific differences in the morphology of CCAOs cultured in dLECM1, dLECM2 or dLECM3 were not observed (Fig. S11). Nevertheless, differences within biological replicates of recellularized dLECM were noticed via microscopy and the transition of culture medium color during culturing (Fig. S12).

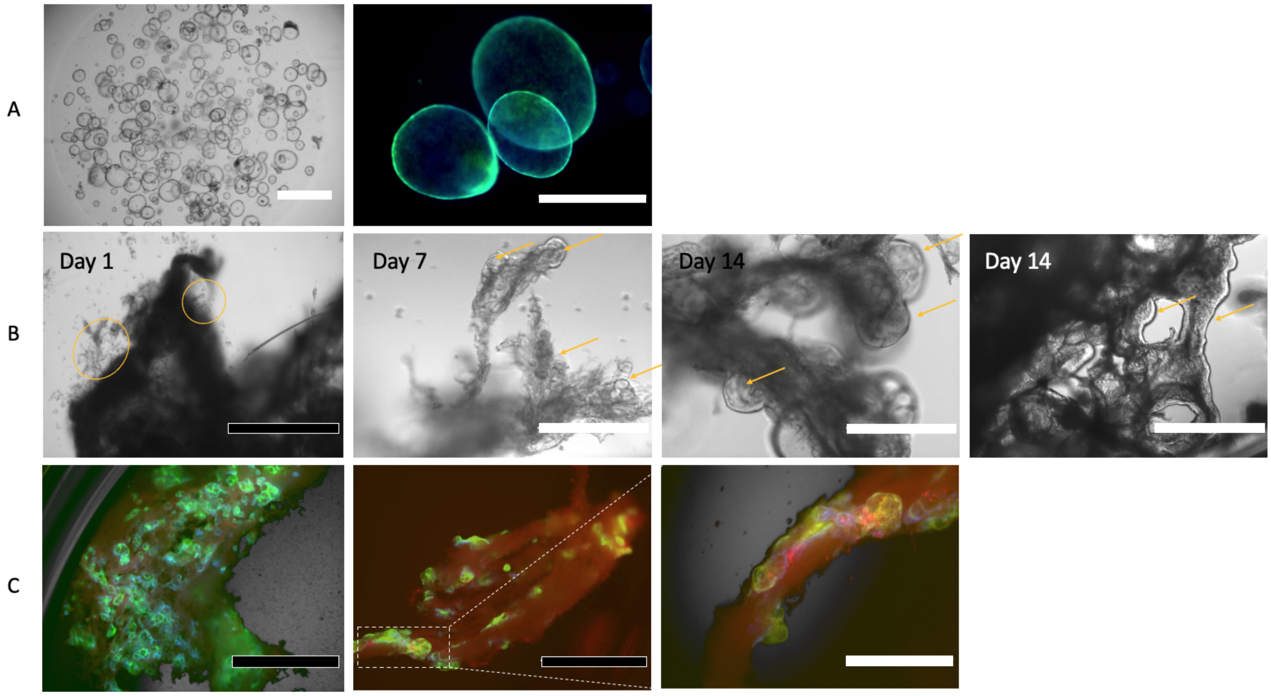

Figure 8: **Adhesion, expansion and survival of CCAOs in dLECM A)** Left: representative bright field microscopy images of CCAO culture (CCAO1, day 3 after passaging). Right: representative image of live/dead staining of CCAOs (CCAO1) grown in BME shows their viability. Scale bars indicate 1000 μm. **B)** Representative bright field microscopy images of CCAOs cultured in dLECM on day 1, 7 and 14 after recellularization. Yellow circles indicate single cells, yellow arrows indicate ingrown and adhered organoids. From left to right: CCAO2+dLECM3, CCAO2+dLECM3, CCAO2+dLECM3, CCAO3+dLECM2. Black scale bar indicates 1000 μm, white scale bars indicate 400 μm. **C)** Representative images of live/dead staining of CCAOs cultured in dLECM on day 15 (left) and day 18 (center, right) after recellularization, showing their viability, dispersion through the scaffold and organoid structure. Left: CCAO1+dLECM2, center and right: CCAO3+dLECM1. Black scale bars indicate 2000 μm, white scale bar indicates 1000 μm.

Metastatic outgrowth of CCAOs is ECM and organoid line dependent

Cell metabolism is a cascade of biochemical reactions that transform metabolites to establish biological functions essential for cell viability. To get insight into the effect of dLECM compared to BME on CCAO cultures in terms of metabolic activity, metabolic assays with PrestoBlue cell viability reagent were performed (Fig. 9, S15). In both recellularized dLECMs (n=27, n=3 ECM donors with n=3 CCAO lines and n=3 biological replicates per combination) as CCAOs cultured in BME (n=3 CCAO lines cultured in BME domes), CCAOs were metabolically active for at least 18 days (Fig. 9A). CCAOs cultured in dLECM showed reduced metabolic activity compared to CCAOs cultured in BME (Fig. 9A). While no significant differences were observed when values from all time points were matched (Fig. 9A), statistically significant differences in metabolic activity were observed when the separate time points were evaluated, starting on day 14 after recellularization (Fig. S15A). The decrease in metabolic activity between days 14 and 18 after recellularization suggests a stagnation in metabolic activity during this period.

Differences in metabolic activity were found when comparing CCAOs cultured in various dLECMs (dLECM1, dLECM2, dLECM3) (Fig. 9B). CCAOs cultured in dLECM3 showed significantly the highest metabolic activity, starting at day 11 after recellularization (Fig. S15B). Figure S16, a detailed version of Figure 9, demonstrates all metabolic activity measurements divided per dLECM and CCAO line. Significant differences were present between the metabolic activity of CCAO1 cultured in dLECM1, dLECM2 and dLECM3 and between CCAO3 cultured in dLECM1, dLECM2 and dLECM3 (Fig. S16a), indicating that the metabolic activity of CCAOs is dictated by the scaffold donor.

Metabolic activity patterns also differ when comparing various CCAO lines (CCAO1, CCAO2, CCAO3) cultured in dLECM (Fig. 9C). CCAO2 showed the lowest overall metabolic activity (Fig. 9C) in the three dLECMs (dLECM1, dLECM2, dLECM3) but also in BME (Fig. S16a, S17), indicating dependency of metabolic activity on organoid line. Thus, results demonstrated that the metabolic activity of CCA organoids is lower in dLECM compared to BME, and is dictated both by the dECM donor and the organoid line. This suggests a significant influence of both the cancer cells as the lung ECM on the metastatic outgrowth of CCA in lung.

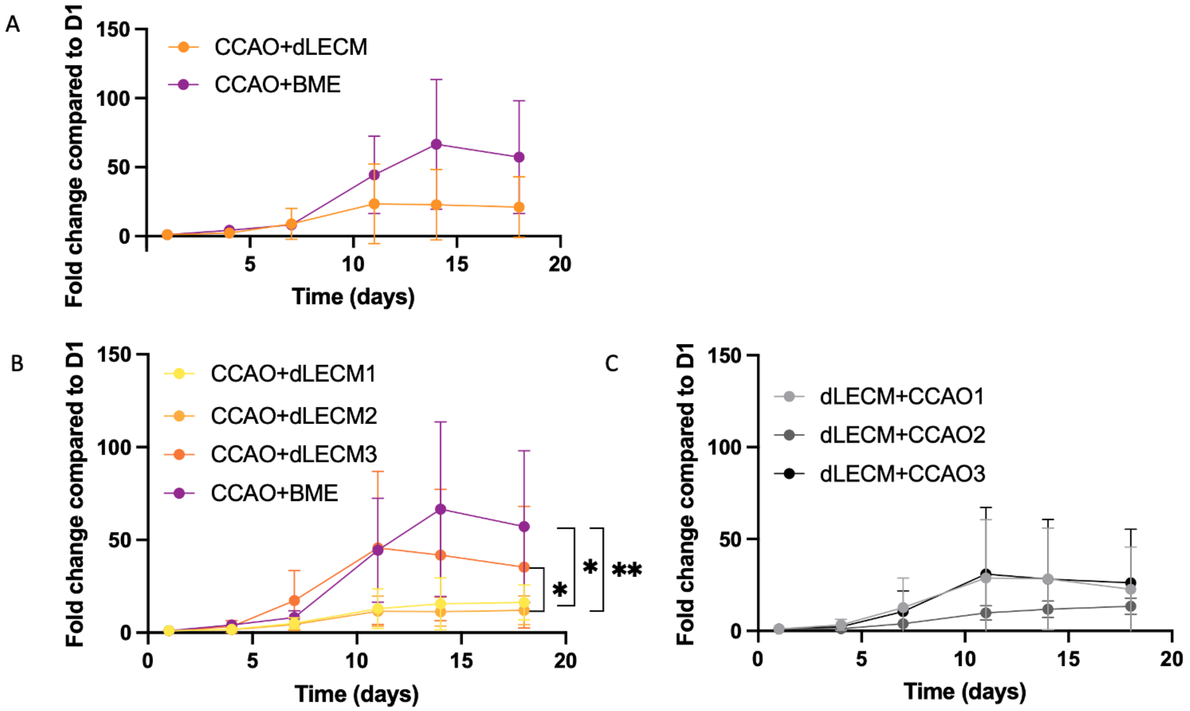

Figure 9: **Metabolic activity of recellularized dLECM with CCAOs during 18 days after recellularization**. **A)** Presto blue measurements of recellularized dLECM (n=27, n=3 ECM donors with n=3 CCAO lines and n=3 biological replicates per combination) and CCAOs in BME (n=3) measured on day 1, 4, 8, 11, 14, 18. Overall higher metabolic activity is shown when CCAOs were cultured in BME (purple) compared to dLECM (orange). No statistical differences were present. Metabolic activity of CCAOs is represented by the fold change relative to day 1 (D1) after recellularization. **B)** Metabolic activity for CCAOs in dLECM split based on scaffold donor (i.e., dLECM1, dLECM2, dLECM3). CCAO lines are combined. Statistical differences were present between CCAOs cultured in dLECM1 and BME (p=0.0168), CCAOs cultured in dLECM2 and BME (p=0.0029), CCAOs cultured in dLECM2 and dLECM3 (p=0.185). **C)** Metabolic activity for CCAOs in dLECM split based on patient origin of CCAO (i.e., CCAO1, CCAO2, CCAO3). dLECM1, dLECM2, dLECM3 are combined. No statistical differences were present between CCAO lines cultured in dLECM. In A, B and C, Two-Way ANOVA statistical test was performed where values of 1 line were matched by the factor time.

Occupation of CCAOs in decellularized lung scaffolds

To image the morphology of the CCAOs attached to the dLECM, actin filaments and nuclear material were stained and captured 18 days after recellularization (Fig. 10A, S18). Staining of the key cytoskeletal component F-actin (phalloidin) showed the organoid-like morphology, confirming previous bright field images (Fig. 8, S11). Additionally, Vimentin, a well-established marker for EMT, showed localized expression [104].

To determine whether the cells were capable of invading into the dLECM, H&E staining of cross-sections of recellularized dLECM were made (Fig. 10B). Monolayers and clusters of cells were found attached to the dLECM. A widespread cellular presence is observed throughout the decellularized scaffold, but a preference of the CCAOs for adhesion to and growth in the macroscopic holes is visible (Fig. 10B,C). This localized colonization and in-growth in the scaffold is similar to a previously depicted *in vivo* growth pattern [105]. The sequence of two-dimensional cross-sections confirmed the occupation and invasion of CCAOs throughout the dLECM at day 18 after recellularization.

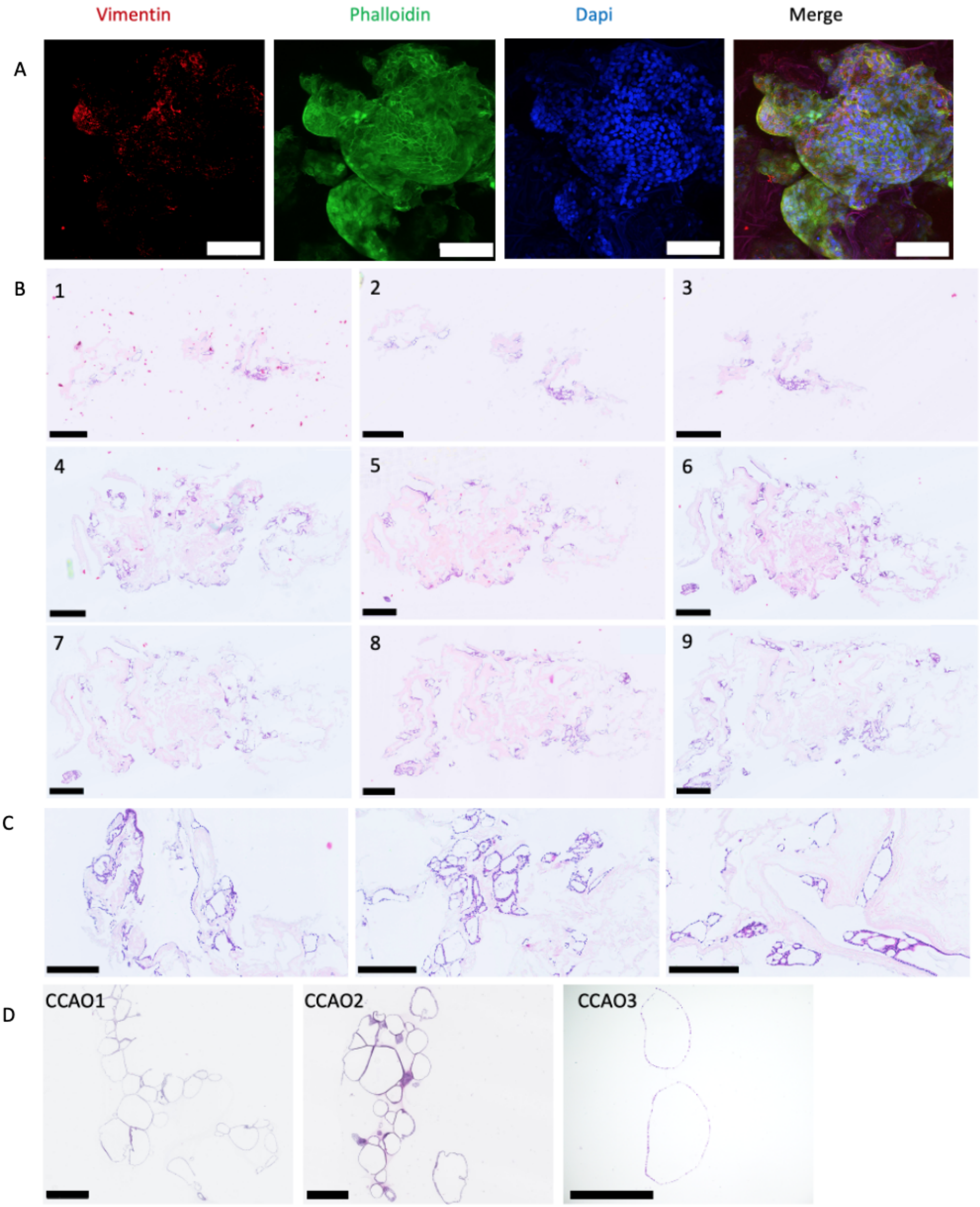

Figure 10: **Occupation and invasion of CCAOs in dLECM. A)** Whole-mount confocal images for Vimentin (red), Phalloidin (green) and DAPI (blue) of CCAO2 in dLECM2 at day 18 after recellularization. Scale bars indicate 100 μm. **B,C)** H&E staining of sectioned dLECM1 recellularized with CCAOs (CCAO2) at multiple intervals from top (1) to bottom (9) showing monolayers and clusters of CCAOs at day 18 after recellularization. Scale bars in B) indicate 500 μm and in C) indicate 250 μm. **D)** H&E staining of sectioned CCAOs showing monolayers and clusters of CCAOs. Scale bars indicate 500 μm.

Gene expression levels of CCAO recellularized lung scaffolds compared to CCAOs cultured in BME

To identify the biological processes that are important for metastasis of CCA in the lung, gene expression profiles of CCAOs cultured in dLECM are determined and compared to matched CCAOs cultured in BME (Fig. 11). Cancer stem cell markers LGR5 and CD133, of which the expression is known to promote tumor growth and heterogeneity, were found to be downregulated compared to matched CCAOs cultured in BME [106, 107]. As expected, the expression of a well-established CCA marker KRT7 was comparable between CCAOs cultured in dLECM and in BME, indicating retention of their CCA phenotype [108]. Additionally, a well-known tumor cell proliferation marker Ki-67 showed downregulation in the dLECM environment compared to BME, which corresponds to metabolic activity assay results (Fig. 9). EMT marker E-cadherin was downregulated when CCAOs were cultured in dLECM in comparison to BME, possibly due to increased occurrence of EMT in the dLECM environment [109, 110, 111]. Classical EMT markers Vimentin and MUC1, and the expression of ECM-related genes collagen type 1 (Col1A1) and Fibronectin showed heterogeneous expression, indicating that both the ECM donor and patient could influence the upregulation of these genes. Collagen type 3 (Col3A1), which overexpression is associated with tumor progression and migration [112], was downregulated when cultured in dLECM. This indicates that the ECM of the metastatic organ affects the mutual production of ECM proteins. Also, the ECM-binding subunits of integrin receptors integrin$\alpha 5$ (Integrin A5) and integrin$\beta 1$ (Integrin B1) showed high heterogeneity, both in expression between different CCAO lines as dLECMs [113]. This suggests that in lung metastasis, upregulation of these genes could be patient and donor ECM dependent. Given the small sample size, no statistical tests were performed. Overall, results indicate differential gene expression levels concerning cancer stem cell markers, a proliferation marker, EMT markers and ECM proteins, between CCAOs cultured in dLECM compared to those cultured in BME. This finding underscores the influence of the culture environment on the gene expression of CCAOs.

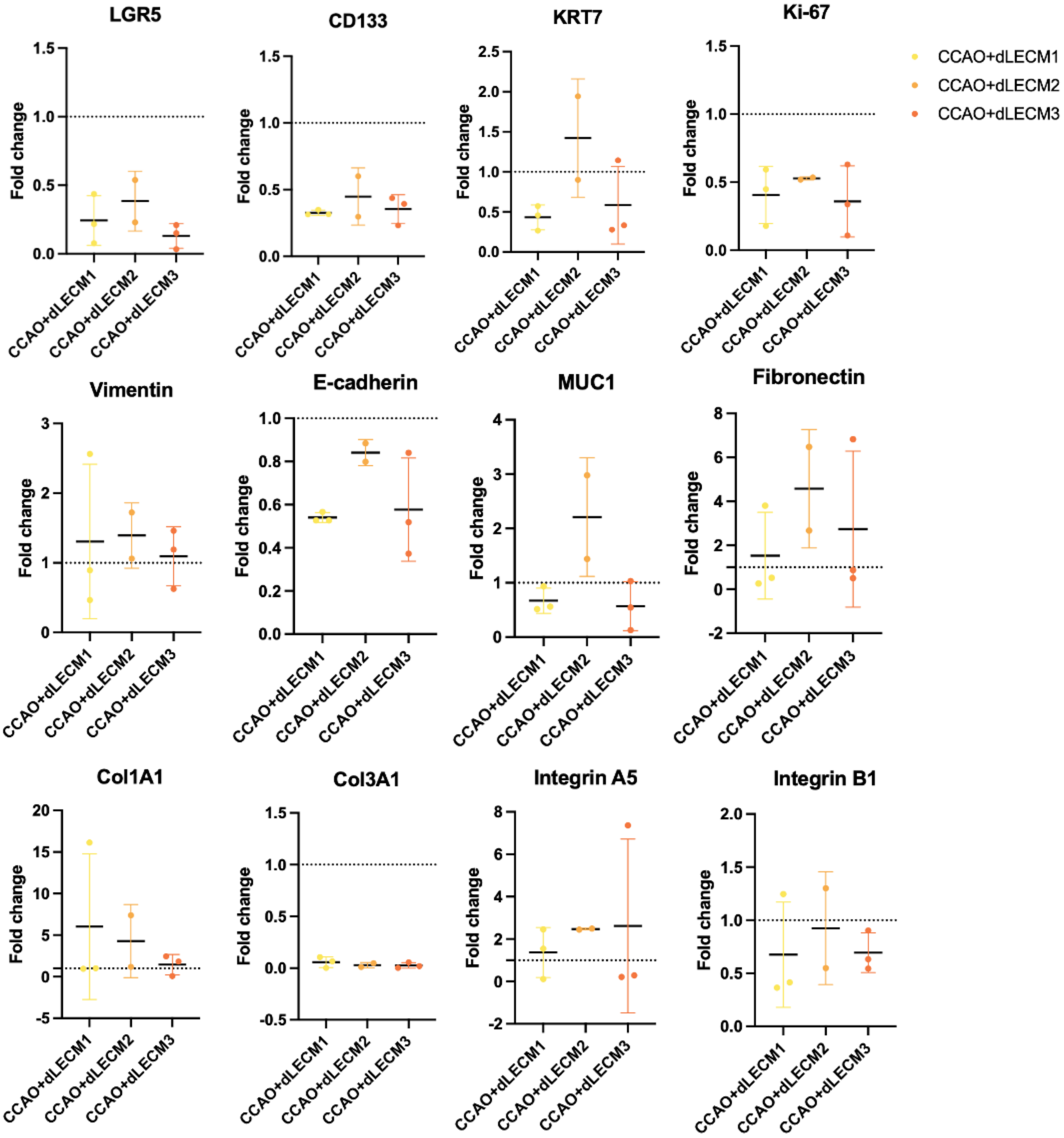

Figure 11: **Gene expression profiles of dLECM recellularized with CCAOs compared to matched CCAOs cultured in BME at day 18 after recellularization.** Fold changes ($2^{-\Delta\Delta Ct}$) of selected genes compared to matched CCAOs grown in BME are presented. GAPDH and HRPT were used as reference genes. CCAOs cultured in dLECM exhibited downregulation of cancer stem cell markers LGR5 and CD133, proliferation marker Ki-67, EMT marker E-cadherin and Collagen type 3, compared to matched CCAOs cultured in BME. CCA marker KRT7, EMT markers Vimentin and MUC1, ECM-related genes Fibronectin and Collagen type 1 and cell-ECM interaction related genes Integrin A5 and Integrin B1, were up- or downregulation for CCAOs cultured in dLECM when compared to matched CCAOs cultured in BME.

Discussion

CCA metastatic models with human-derived ECM of target organs for metastasis are lacking, whereas the role of the ECM in cancer metastasis is crucial [114]. Particularly, the interplay between cancer cells and the ECM within the metastatic organ contributes to the dynamics of metastatic colonization [115, 116]. In this study, we demonstrated the capability to decellularize human-derived tissue of common distant metastatic locations for CCA, lung and lymph node, and revealed biomechanical and biochemical characteristics of the dLECM and dNECM which recapitulated the tissue of origin. Additionally, as a proof-of-concept, patient-derived CCAOs were cultured in dLECM to model metastatic colonization of CCA in the lungs *in vitro*, to understand the role of the ECM in metastatic outgrowth. The dLECM supported the adhesion, invasion and culture of CCAOs. The metastatic outgrowth of CCAOs in dLECM was dictated by both the CCAO line, representing the tumor itself, as well as the dLECM donor, representing the ECM of the target organ. CCAOs cultured in dLECM showed lower metabolic activity and differential gene expression profiles compared to CCAOs cultured in BME.

The decellularization method used in this study, utilizing TX-100, successfully removed cellular material from both human lung and lymph node tissue. The decellularization of human lymph nodes has not yet been reported in the literature. Established requirements for complete cell removal after decellularization were met and essential ECM components, including collagens and sGAGs, were retained. The decrease in DNA content and retention of ECM components between dLECM and dNECM were similar, but differences in tissue structure and the presence of collagen were noticed. The loss of sGAGs after decellularization might be due to the loss of intracellular sGAG-interacting proteins while the extracellular sGAG-interacting proteins were preserved, since the used sGAG assay did not differentiate between these two types of sGAGs [117]. Two lymph nodes did not meet the threshold of <50 ng DNA/mg wet tissue, which could be ascribed to their relatively greater dimensions compared to the other lymph nodes and might need more TX-100 decellularization cycles. The inaccuracy of the Nanodrop for relatively small amounts may also have played a role.

The mechanical role of the ECM in cancer metastasis is complicated due to the interaction of numerous factors. Matrix stiffness, but also pore size, viscoelasticity, fiber network configuration, crosslinking proteins, density and cancer cell stiffness are players in the biophysical interactions between cancer cells and their environment [118, 119]. These factors, in turn, effect matrix remodeling, cell spreading, migration and differentiation of cells [65]. Therefore, biomechanical characterization of the decellularized tissues was performed to eventually augment understanding of the reciprocal relationship between the ECM stiffness and the outgrowth of cancer cells. Similar macro- and micro-scale stiffness for dLECM and dNECM were obtained, with a notable variability in the macro-scale stiffness between dNECMs. The variability in macro-scale stiffness of dLECMs and dNECMs can be attributed not only to the biological variability of lungs and lymph nodes, but also to their exact locations of origin in the human body, which are unknown for both tissue types [120]. To note, during rheology measurements, the dLECMs were only $400\mu m$ thick, but the contact point was found at a gap ≥ 1.1 mm. This may be due to tissue folding or the dLECM being swollen between cutting and placement on the rheometer, but it should not affect the results. The heterogeneity in the micro-scale stiffness was expected because of the structure of the alveolar septa in lung, and the differences in pore size and reticular meshwork in lymph nodes (Fig. 5A, 6C,D) [88, 121]. Although the obtained mechanical properties (Young's modulus) of dLECM are comparable to literature, these properties are only known for animal-derived dLECM, non-decellularized human ECM or engineered hydrogels, clarifying the relevance of this study (Table S5, S6). Mechanical characterization of human dNECM is absent in the literature.

This study demonstrated that patient-derived CCAOs can be cultured in dLECM to create an *in vitro* model encompassing both cellular and environmental aspects of metastatic colonization of CCA in the lungs. The model exhibited biocompatibility, adherence, growth, and metabolic activity of CCAOs in dLECMs. As anticipated, CCAOs cultured in dLECM exhibited significantly lower metabolic activity compared to those cultured in BME, confirming the significance of the enhanced model. This observed difference can be attributed to the bioactive micro-environment and growth factors provided by BME that promote cell viability. To note, differences were obtained in PrestoBlue measurements and expansion (bright field images and microscopic observations) between biological replicates (Fig. S12). However, we limited the variability in PrestoBlue measurements by using multiple donors for the lung and multiple CCAO lines. Donor-dependent metabolic activity was observed, with dLECM3 favoring the metabolic activity of CCAO1 and CCAO3 compared to dLECM1 and dLECM2. To note, dLECM3 was obtained from a current smoker, which is in contrast to the other two donors (former smoker <10 years and never smoke). Although the relationship between smoking and metastasis of CCA to lung has not been studied, previous studies have shown that smoking contributes to the initiation and progression of other types of cancers such as soft tissue sarcoma, esophageal cancer, breast cancer and colorectal cancer [122, 123, 124, 125]. Further research is necessary to establish a direct relationship between smoking and metastasis of CCA to the lungs, given the dependence on multiple variables.

Discussing the normalized metabolic activity assay data, the results indicate that CCAO2 is the least metabolically active (Fig. S17, right). However, zooming in on the absolute values of CCAO2 (Fig. S17, left), these indicate that the metabolic activity of CCAO2 had already higher absolute values at day 1 and day 4 after recellularization compared to CCAO1 and CCAO3. This can be due to the longer time taken by CCAO1 and CCAO3 to pave their way into the dLECM or for the switch from a dormant to a proliferative phenotype in the new environment, indicating organoid line dependent outgrowth.

Gene expression profiles of dLECM recellularized with CCAOs expressed up- or downregulated genes in comparison to CCAOs cultured in BME. The differences between BME and dECM scaffold cultures in structure (hydrogel versus scaffold), growth dimension (3D versus 2.5D), and components, likely had a significant impact on the observed gene expression. Notably, cancer stem cell markers LGR5 and CD133, and EMT marker E-cadherin, showed downregulation when CCAOs were cultured in dLECM compared to BME. LGR5 and CD133 expression in CCA may also be associated with EMT [126, 127]. Therefore, our findings suggest that the extent of EMT is dependent on the microenvironment of the CCAO cultures, and should be taken into account in an *in vitro* model for metastasized CCA. While no clear pattern of up- or downregulation was observed for the EMT marker Vimentin in recellularized dLECMs compared to CCAOs cultured in BME, its expression in the former corresponds to the visible Vimentin expression in whole-mount confocal imaging. Overall, the up-or downregulation of the genes KRT7, Vimentin, MUC1, Fibronectin, Collagen type 1, Integrin A5 and Integrin B1 in CCAOs cultured in dLECM compared to BME was heterogeneous, both in expression between different CCAO lines and dLECMs, making it difficult to draw firm conclusions. Also, qPCR results from only two dLECMs (dLECM1 and dLECM3) were included in the analysis of CCAO3 cultures, due to the undetermined Ct values for CCAO3 cultured in dLECM2 for unknown reasons. Gaining gene expression profiles at earlier time points after recellularization, in addition to day 18, may aid in the understanding of the biological interactions between CCAOs and dLECM.

To build upon the findings, future research is required, beginning with revising and optimizing the decellularization method. According to the literature, TX-100 is more efficient and less damaging and cytotoxic than alternatives used for decellularization such as sodium dodecyl sulfate (SDS), sodium deoxycholate (SD), CHAPS, NaOH and Trypsin/EDTA [89, 90]. However, there is currently no unequivocal optimal method known for the decellularization of lung and lymph nodes, let alone specifically for human-derived lymph nodes and 400μm thick human-derived lung slices [88, 89, 128, 129, 130]. Conclusions in literature on decellularization methods often rely on animal-derived tissue, which may be representative but not fully analogous to human-derived tissue [131]. Although the decellularization method employed was sufficient, it could be improved in terms of optimizing speed, efficiency, slice thickness, and minimizing the use of harsh detergents. The effect of decellularization detergents may vary depending on the thickness of the slices and the duration of exposure [128], thus highlighting the need for future research to identify an optimal decellularization method for human lung slices and lymph nodes.

Decellularization methods and tissue section thickness can potentially impact biochemical and biomechanical characteristics, such as composition and stiffness of the dECM [132, 133]. While Melo et al. (2014) found that various decellularization methods did not significantly alter the local stiffness of dLECM, this has yet to be investigated in relation to lymph nodes and the impact of tissue thickness [120]. Further research can investigate the mechanical properties of the dECM resulting from different decellularization methods and tissue thickness to optimize the recapitulation of *in vivo* ECM. Furthermore, decellularization of human lung and lymph nodes has potential beyond facilitating the modeling of CCA metastatic colonization. This includes the development of disease models for lung and lymph nodes, the production of tissue scaffolds using bioprinting, and tissue engineering [134].

Through characterization of the macro- and micro-scale stiffness of human dLECM and dNECM, this study provides a partial understanding of the mechanical properties of these scaffolds. However, a comprehensive assessment of the mechanical properties, including porosity and fiber network configuration, requires further investigation. Although hydrogels do not perfectly replicate the unique ECM composition of the tissue being mimicked, future studies could use polyethylene glycol or polyacrylamide gels with a (tunable) stiffness adjusted to the ECM of the metastatic location. Combining these gels with CCAOs may help elucidate the complex and multifactorial role of the ECM in cancer metastasis. For instance, previous studies have investigated the stiffness-mediated responses of mouse breast cancer cells, paradigms of morphogenesis of intestinal organoids embedded in PEG-based hydrogels, and the upregulation of a mechanoresponsive pathway in hepatocellular carcinoma metastasis due to high matrix stiffness by utilizing mechanically tunable polyacrylamide gels [135, 136, 137]. The performed mechanical characterization can serve as preliminary work for future research into the development of dLECM and dNECM stiffness in response to recellularization with CCAOs.

Based on metabolic activity measurements, our study suggests that both dLECM donor variations and CCAO lines influence the viability of CCAOs in dLECM, possibly due to genetic variations within CCAO lines and variations in dLECM composition. To better understand whether and why CCAOs prefer a specific scaffold for migration and colonization, larger sample sizes (dLECM: $N>3$, CCAOs: $N>3$) and extended gene expression analysis are needed. Further analysis of (recellularized) dECMs using mass spectrometry and matrisome techniques, as well as RNA sequencing, could enhance our understanding of the underlying mechanisms between the ECM and cancer cells in metastasized CCA. Although metabolic activity of recellularized dLECM was compared with CCAOs cultured in BME, BME is less stiff, dense and porous than dLECM, making it easier for organoids to invade and grow [138, 139]. Therefore, future research should investigate the influence of organ-specific acellular scaffolds on CCAOs by comparing their metabolic activity in dLECM with acellular scaffolds of other metastatic organs, such as lymph nodes, instead of BME. The underlying mechanism of organoid migration into the scaffolds can be investigated by using GFP-tagged organoids [140, 141, 79]. Furthermore, it is recommended to use CCAOs with lower passage numbers to avoid potential influence on results due to high passage numbers (>140) of the CCAOs used in the present study.

To gain a more comprehensive understanding of the metabolic activity of CCAOs in dLECM, it is important to acknowledge the potential limitations and biases of the methods used. While the PrestoBlue assay used in this study is a commonly used and effective approach for measuring cell viability, it has been reported to be toxic to some types of tumor cell lines [142]. To overcome these limitations and potential biases, additional metabolic activity assays can be considered alongside PrestoBlue.

Within the created model, the dLECM acts as a pre-metastatic niche. This niche affects colonization, adhesion, differentiation but also proliferation of the tumor cells *in vivo*, according to the literature [116]. In our model, a pre-metastatic niche was absent. This could be incorporated by first introducing immune cells and cancer cell-derived extracellular vesicles (EV), followed by recellularization with CCAOs to investigate if recapitulation of a pre-metastatic niche using this approach, promotes CCAO growth [143, 144]. EVs secreted from cancer cells play a critical role in multiple steps from oncogenesis to early metastasis, including the generation of a pre-metastatic niche [145, 146]. Immune system components are essential to find drug targets and develop therapies eventually, and can be integrated in the designed model utilizing a recently established co-culture method of CCAOs and immune cells [147].

Recently, more research has focused on developing a tumor-microenvironment-on-a-chip, metastasis-on-a-chip [148, 149] and immune-organs-on-a-chip platforms [150], to recapitulate and understand the interaction between the tumor, TME and the immune system. Microfluidic device addition could reconstruct physiological dynamic characteristics in tissue in a controllable environment, similar to Wang et al. (2020) performed for the progression of kidney cancer in the liver [141]. The combination of dECM with tumor organoids used in this study can serve as a foundation for the future development of a CCA-metastasis-on-a-chip model. Such a microfluidic device has the potential to facilitate the mechanistic study of cancer metastasis *in vitro*, enabling the screening of anti-cancer drugs and the development of therapies.

The ultimate goal is to eventually personalize CCA and CCA metastasis treatment to increase the patient survival rate and reduce patient burden. The established model in this study does not provide a patient-specific model encompassing both CCAOs and ECM material from the same donor. Instead, this model demonstrates that by combining dECM of the metastatic location and CCA organoids, avenues are opened to study the interaction of primary epithelial CCA cells and their metastatic ECM environment using human-derived tissue. If practically feasible, combining both immune cells, EVs, CCAOs and ECM material from the same donor would be optimal for the creation of a patient-specific *in vitro* model. The experimental set-up of this study can be applied to other tissue types. In the short term, the developed model is not intended to replace animal models, but rather to complement them in CCA metastasis research. Elucidating the interplay between tumor organoids and tissue-specific decellularized scaffolds *in vitro*, may lead to more effective (ECM-)targeting therapies for patients with metastasized CCA. The application of the three R's principle (reduction, replacement, and refinement) in animal studies is consistent with ethical considerations and promotes exploring alternative systems, such as *in vitro* models [151]. Therefore, the combination of patient-derived CCAOs and human-derived dECMs of metastatic locations presents a promising avenue for scientific inquiry that may reduce reliance on animal models.

Conclusion

Acellular scaffolds of human-derived lung and lymph nodes were successfully obtained via decellularization. Biochemical and biomechanical characterization has demonstrated the preservation of tissue-specific characteristics and has enhanced the understanding of the mechanical properties of dLECM and dNECM. As a proof-of-concept, this study showed the adherence, growth and metabolic activity of CCAOs in dLECM, valuable for creating an *in vitro* model for the metastatic outgrowth of CCA in lung. CCAOs cultured in dLECM exhibited lower metabolic activity compared to CCAOs cultured in BME and the viability of CCAOs was dictated both by the scaffold donor as the organoid line. Furthermore, the differences in gene expression levels of CCAOs cultured in these two different culture environments, dLECM and BME, stress the importance of incorporating the ECM of the metastatic location in an *in vitro* model. Converging patient-derived organoids with organ-specific human-derived dECM, provides a valuable tool for integrating the ECM of the metastatic location to probe interactions between the ECM and the primary epithelial CCA cells in a metastatic setting.

Acknowledgements

I want to thank my daily supervisor MSc. Gilles van Tienderen for his good guidance during the project. I learned a lot from him, theoretically and practically in the lab. His advice and suggestions were very helpful to me during the project. Furthermore, I would like to extend my special thanks to Dr. ir. E.L. Fratila-Apachitei and M.M.A. Verstegen for their excellent support and valuable contributions to this project. Their feedback on my report and insightful discussions about the project were greatly appreciated.
I would like to express my gratitude to the examination committee members, Prof. dr. A.A. Zadpoor, Dr. E.C.M. Carroll and Dr. M.J. Mirzaali Mazandarani for taking the time to review and evaluate my thesis and attend the defense. The entire project could not have been realized without the help of Ir. Eline van Hengel, Dr. Jorke Willemse, Kübra Köten, MSc. Kimberley Ober, Dr. Henk Roest and M.D. Ivo Schurink in the Erasmus MC laboratory under the supervision of Prof. dr. Luc van der Laan, and Ir. James Conboy and Dr. Iain Muntz in the TU Delft laboratory under the supervision of Prof. dr. Gijsje Koenderink. Finally, I would like to thank my boyfriend, family, friends and colleagues of NbEe8 for their support and contribution to how I experienced my graduation period.

References

[1] J. M. Banales, J. J. Marin, A. Lamarca, P. M. Rodrigues, S. A. Khan, L. R. Roberts, V. Cardinale, G. Carpino, J. B. Andersen, C. Braconi, *et al.*, “Cholangiocarcinoma 2020: the next horizon in mechanisms and management,” *Nature Reviews Gastroenterology & Hepatology*, vol. 17, no. 9, pp. 557–588, 2020.

[2] P. Bertuccio, M. Malvezzi, G. Carioli, D. Hashim, P. Boffetta, H. B. El-Serag, C. La Vecchia, and E. Negri, “Global trends in mortality from intrahepatic and extrahepatic cholangiocarcinoma,” *Journal of hepatology*, vol. 71, no. 1, pp. 104–114, 2019.

[3] C. X. Chamberlain, E. Faust, D. Goldschmidt, N. Webster, A. N. Boscoe, D. Macaulay, and M. L. Peters, “Burden of illness for patients with cholangiocarcinoma in the united states: a retrospective claims analysis,” *Journal of Gastrointestinal Oncology*, vol. 12, no. 2, p. 658, 2021.

[4] N. Howlader, A. Noone, M. Krapcho, J. Garshell, D. Miller, S. Altekruse, *et al.*, “Surveillance, epidemiology, and end results (seer) program (www. seer. cancer. gov) seer stat database: Incidence-seer 18 regs research data+ hurricane katrina impacted louisiana cases, nov 2015 sub (20 0 0-2013)< katrina/rita population adjustment>-linke. 2015,” *Rita population adjustment> e Linke*, 2015.

[5] J. M. Banales, V. Cardinale, G. Carpino, M. Marzioni, J. B. Andersen, P. Invernizzi, G. E. Lind, T. Folseraas, S. J. Forbes, L. Fouassier, *et al.*, “Expert consensus document: Cholangiocarcinoma: current knowledge and future perspectives consensus statement from the european network for the study of cholangiocarcinoma (ens-cca),” *Nature reviews. Gastroenterology & hepatology*, vol. 13, no. 5, pp. 261–280, 2016.

[6] G. L. Tyson and H. B. El-Serag, “Risk factors for cholangiocarcinoma,” *Hepatology*, vol. 54, no. 1, pp. 173–184, 2011.

[7] S. Mosadeghi, B. Liu, T. Bhuket, and R. J. Wong, “Sex-specific and race/ethnicity-specific disparities in cholangiocarcinoma incidence and prevalence in the usa: An updated analysis of the 2000–2011 surveillance, epidemiology and end results registry,” *Hepatology Research*, vol. 46, no. 7, pp. 669–677, 2016.

[8] M. M. Kirstein and A. Vogel, “Epidemiology and risk factors of cholangiocarcinoma,” *Visceral medicine*, vol. 32, no. 6, pp. 395–400, 2016.

[9] Y. Nakanuma, Y. Sato, K. Harada, M. Sasaki, J. Xu, and H. Ikeda, “Pathological classification of intrahepatic cholangiocarcinoma based on a new concept,” *World journal of hepatology*, vol. 2, no. 12, p. 419, 2010.

[10] T. Patel, “Cholangiocarcinoma,” *Nature clinical practice Gastroenterology & hepatology*, vol. 3, no. 1, pp. 33–42, 2006.

[11] O. Clements, J. Eliahoo, J. U. Kim, S. D. Taylor-Robinson, and S. A. Khan, “Risk factors for intrahepatic and extrahepatic cholangiocarcinoma: a systematic review and meta-analysis,” *Journal of hepatology*, vol. 72, no. 1, pp. 95–103, 2020.

[12] Y. H. Shaib, H. B. El-Serag, J. A. Davila, R. Morgan, and K. A. McGlynn, “Risk factors of intrahepatic cholangiocarcinoma in the united states: a case-control study,” *Gastroenterology*, vol. 128, no. 3, pp. 620–626, 2005.

[13] A. G. Singal, M. O. Rakoski, R. Salgia, S. Pelletier, T. H. Welling, R. J. Fontana, A. Lok, and J. A. Marrero, “The clinical presentation and prognostic factors for intrahepatic and extrahepatic cholangiocarcinoma in a tertiary care centre,” *Alimentary pharmacology & therapeutics*, vol. 31, no. 6, pp. 625–633, 2010.

[14] D. Alvaro, M. C. Bragazzi, A. Benedetti, L. Fabris, G. Fava, P. Invernizzi, M. Marzioni, G. Nuzzo, M. Strazzabosco, T. Stroffolini, *et al.*, “Cholangiocarcinoma in italy: A national survey on clinical characteristics, diagnostic modalities and treatment. results from the “cholangiocarcinoma” committee of the italian association for the study of liver disease,” *Digestive and Liver Disease*, vol. 43, no. 1, pp. 60–65, 2011.

[15] D. Adams, R. Alteri, and M. Anand, “Cancer facts amp; figures 2022,” 2022.

[16] D. Walter, C. Döring, M. Feldhahn, F. Battke, S. Hartmann, R. Winkelmann, M. Schneider, K. Bankov, A. Schnitzbauer, S. Zeuzem, *et al.*, "Intratumoral heterogeneity of intrahepatic cholangiocarcinoma," *Oncotarget*, vol. 8, no. 9, p. 14957, 2017.

[17] Y. A. Ghouri, I. Mian, and B. Blechacz, "Cancer review: cholangiocarcinoma," *Journal of carcinogenesis*, vol. 14, 2015.

[18] G. S. van Tienderen, B. Groot Koerkamp, J. N. IJzermans, L. J. van der Laan, and M. M. Verstegen, "Recreating tumour complexity in a dish: Organoid models to study liver cancer cells and their extracellular environment," *Cancers*, vol. 11, no. 11, p. 1706, 2019.

[19] P. J. Brindley, M. Bachini, S. I. Ilyas, S. A. Khan, A. Loukas, A. E. Sirica, B. T. Teh, S. Wongkham, and G. J. Gores, "Cholangiocarcinoma," *Nature Reviews Disease Primers*, vol. 7, no. 1, pp. 1–17, 2021.

[20] J. L. van Vugt, M. P. Gaspersz, R. J. Coelen, J. Vugts, T. A. Labeur, J. de Jonge, W. G. Polak, O. R. Busch, M. G. Besselink, J. N. IJzermans, *et al.*, "The prognostic value of portal vein and hepatic artery involvement in patients with perihilar cholangiocarcinoma," *Hpb*, vol. 20, no. 1, pp. 83–92, 2018.

[21] A. K. Gravely, E. Vibert, and G. Sapisochin, "Surgical treatment of intrahepatic cholangiocarcinoma," *Journal of Hepatology*, vol. 77, no. 3, pp. 865–867, 2022.

[22] B. Blechacz, "Cholangiocarcinoma: current knowledge and new developments," *Gut and liver*, vol. 11, no. 1, p. 13, 2017.

[23] F. Hahn, L. Müller, A. Mähringer-Kunz, Y. Tanyildizi, D. P. d. Santos, C. Düber, P. R. Galle, A. Weinmann, and R. Kloeckner, "Distant metastases in patients with intrahepatic cholangiocarcinoma: does location matter? a retrospective analysis of 370 patients," *Journal of oncology*, vol. 2020, 2020.

[24] X. Wang, G.-Y. Yu, M. Chen, R. Wei, J. Chen, and Z. Wang, "Pattern of distant metastases in primary extrahepatic bile-duct cancer: A seer-based study," *Cancer medicine*, vol. 7, no. 10, pp. 5006–5014, 2018.

[25] W. Wu, X. He, D. Andayani, L. Yang, J. Ye, Y. Li, Y. Chen, and L. Li, "Pattern of distant extrahepatic metastases in primary liver cancer: a seer based study," *Journal of Cancer*, vol. 8, no. 12, p. 2312, 2017.

[26] X. Yan, P. Wang, Z. Zhu, Z. Ning, L. Xu, L. Zhuang, J. Sheng, and Z. Meng, "Site-specific metastases of intrahepatic cholangiocarcinoma and its impact on survival: a population-based study," *Future Oncology*, vol. 15, no. 18, pp. 2125–2137, 2019.

[27] R. Cheng, Q. Du, J. Ye, B. Wang, and Y. Chen, "Prognostic value of site-specific metastases for patients with advanced intrahepatic cholangiocarcinoma: A seer database analysis," *Medicine*, vol. 98, no. 49, 2019.

[28] B. Groot Koerkamp, J. K. Wiggers, P. J. Allen, O. R. Busch, M. I. D'Angelica, R. P. DeMatteo, Y. Fong, M. Gonen, D. J. Gouma, T. P. Kingham, *et al.*, "American joint committee on cancer staging for resected perihilar cholangiocarcinoma: a comparison of the 6th and 7th editions," *HPB*, vol. 16, no. 12, pp. 1074–1082, 2014.

[29] S. Kizy, A. M. Altman, S. Marmor, K. Wirth, J. Y. C. Hui, T. M. Tuttle, J. W. Denbo, and E. H. Jensen, "Surgical resection of lymph node positive intrahepatic cholangiocarcinoma may not improve survival," *HPB*, vol. 21, no. 2, pp. 235–241, 2019.

[30] J. I. Lee and J. S. Campbell, "Role of desmoplasia in cholangiocarcinoma and hepatocellular carcinoma," *Journal of Hepatology*, vol. 61, no. 2, pp. 432–434, 2014.

[31] A. E. Sirica and G. J. Gores, "Desmoplastic stroma and cholangiocarcinoma: clinical implications and therapeutic targeting," *Hepatology (Baltimore, Md.)*, vol. 59, no. 6, p. 2397, 2014.

[32] A. E. Sirica, D. J. Campbell, and C. I. Dumur, "Cancer-associated fibroblasts in intrahepatic cholangiocarcinoma," *Current Opinion in Gastroenterology*, vol. 27, no. 3, pp. 276–284, 2011.

[33] S.-i. Aishima, K.-i. Taguchi, T. Terashi, S. Matsuura, M. Shimada, and M. Tsuneyoshi, “Tenascin expression at the invasive front is associated with poor prognosis in intrahepatic cholangiocarcinoma,” *Modern pathology*, vol. 16, no. 10, pp. 1019–1027, 2003.

[34] D. Høgdall, M. Lewinska, and J. B. Andersen, “Desmoplastic tumor microenvironment and immunotherapy in cholangiocarcinoma,” *Trends in Cancer*, vol. 4, no. 3, pp. 239–255, 2018.

[35] J. Vaquero, N. Guedj, A. Clapéron, T. H. N. Ho-Bouldoires, V. Paradis, and L. Fouassier, “Epithelial-mesenchymal transition in cholangiocarcinoma: From clinical evidence to regulatory networks,” *Journal of hepatology*, vol. 66, no. 2, pp. 424–441, 2017.

[36] M. Cadamuro, G. Nardo, S. Indraccolo, L. Dall’Olmo, L. Sambado, L. Moserle, I. Franceschet, M. Colledan, M. Massani, T. Stecca, *et al.*, “Platelet-derived growth factor-d and rho gtpases regulate recruitment of cancer-associated fibroblasts in cholangiocarcinoma,” *Hepatology*, vol. 58, no. 3, pp. 1042–1053, 2013.

[37] B. D. Hedley and A. F. Chambers, “Tumor dormancy and metastasis,” *Advances in cancer research*, vol. 102, pp. 67–101, 2009.

[38] J. S. Di Martino, A. R. Nobre, C. Mondal, I. Taha, E. F. Farias, E. J. Fertig, A. Naba, J. A. Aguirre-Ghiso, and J. J. Bravo-Cordero, “A tumor-derived type iii collagen-rich ecm niche regulates tumor cell dormancy,” *Nature cancer*, vol. 3, no. 1, pp. 90–107, 2022.

[39] F. Kai, A. P. Drain, and V. M. Weaver, “The extracellular matrix modulates the metastatic journey,” *Developmental cell*, vol. 49, no. 3, pp. 332–346, 2019.

[40] J. Fares, M. Y. Fares, H. H. Khachfe, H. A. Salhab, and Y. Fares, “Molecular principles of metastasis: a hallmark of cancer revisited,” *Signal transduction and targeted therapy*, vol. 5, no. 1, p. 28, 2020.

[41] A. Sontheimer-Phelps, B. A. Hassell, and D. E. Ingber, “Modelling cancer in microfluidic human organs-on-chips,” *Nature Reviews Cancer*, vol. 19, no. 2, pp. 65–81, 2019.

[42] E. Hirata and E. Sahai, “Tumor microenvironment and differential responses to therapy,” *Cold Spring Harbor perspectives in medicine*, vol. 7, no. 7, p. a026781, 2017.

[43] A. Jusakul, I. Cutcutache, C. H. Yong, J. Q. Lim, M. N. Huang, N. Padmanabhan, V. Nellore, S. Kongpetch, A. W. T. Ng, L. M. Ng, *et al.*, “Whole-genome and epigenomic landscapes of etiologically distinct subtypes of cholangiocarcinomaintegrative genomic and epigenomic analysis of cholangiocarcinoma,” *Cancer discovery*, vol. 7, no. 10, pp. 1116–1135, 2017.

[44] L. Dai, W. Hu, Z. Yang, D. Chen, B. He, Y. Chen, L. Zhou, H. Xie, J. Wu, and S. Zheng, “Upregulated expression of hoxb7 in intrahepatic cholangiocarcinoma is associated with tumor cell metastasis and poor prognosis,” *Laboratory Investigation*, vol. 99, no. 6, pp. 736–748, 2019.

[45] R. L. Smoot, N. W. Werneburg, T. Sugihara, M. C. Hernandez, L. Yang, C. Mehner, R. P. Graham, S. F. Bronk, M. J. Truty, and G. J. Gores, “Platelet-derived growth factor regulates yap transcriptional activity via src family kinase dependent tyrosine phosphorylation,” *Journal of cellular biochemistry*, vol. 119, no. 1, pp. 824–836, 2018.

[46] M. Kapałczyńska, T. Kolenda, W. Przybyła, M. Zajączkowska, A. Teresiak, V. Filas, M. Ibbs, R. Bliźniak, Ł. Łuczewski, and K. Lamperska, “2d and 3d cell cultures–a comparison of different types of cancer cell cultures,” *Archives of Medical Science*, vol. 14, no. 4, pp. 910–919, 2018.

[47] J. L. Leiting, S. J. Murphy, J. R. Bergquist, M. C. Hernandez, T. Ivanics, A. M. Abdelrahman, L. Yang, I. Lynch, J. B. Smadbeck, S. P. Cleary, *et al.*, “Biliary tract cancer patient-derived xenografts: Surgeon impact on individualized medicine,” *JHEP Reports*, vol. 2, no. 2, p. 100068, 2020.

[48] G. Cavalloni, C. Peraldo-Neia, C. Varamo, L. Casorzo, C. Dell’Aglio, P. Bernabei, G. Chiorino, M. Aglietta, and F. Leone, “Establishment and characterization of a human intrahepatic cholangiocarcinoma cell line derived from an italian patient,” *Tumor Biology*, vol. 37, no. 3, pp. 4041–4052, 2016.

[49] M. Hidalgo, F. Amant, A. V. Biankin, E. Budinská, A. T. Byrne, C. Caldas, R. B. Clarke, S. de Jong, J. Jonkers, G. M. Mælandsmo, *et al.*, "Patient-derived xenograft models: an emerging platform for translational cancer research," *Cancer discovery*, vol. 4, no. 9, pp. 998–1013, 2014.

[50] Y. Gao, R. Zhou, J.-F. Huang, B. Hu, J.-W. Cheng, X.-W. Huang, P.-X. Wang, H.-X. Peng, W. Guo, J. Zhou, *et al.*, "Patient-derived xenograft models for intrahepatic cholangiocarcinoma and their application in guiding personalized medicine," *Frontiers in Oncology*, vol. 11, 2021.

[51] S. Mancarella, G. Serino, F. Dituri, A. Cigliano, S. Ribback, J. Wang, X. Chen, D. F. Calvisi, and G. Giannelli, "Crenigacestat, a selective notch1 inhibitor, reduces intrahepatic cholangiocarcinoma progression by blocking vegfa/dll4/mmp13 axis," *Cell Death & Differentiation*, vol. 27, no. 8, pp. 2330–2343, 2020.

[52] F. Song, B. Hu, J.-W. Cheng, Y.-F. Sun, K.-Q. Zhou, P.-X. Wang, W. Guo, J. Zhou, J. Fan, Z. Chen, *et al.*, "Anlotinib suppresses tumor progression via blocking the vegfr2/pi3k/akt cascade in intrahepatic cholangiocarcinoma," *Cell death & disease*, vol. 11, no. 7, p. 573, 2020.

[53] S. Brun, F. Bassissi, C. Serdjebi, M. Novello, J. Tracz, F. Autelitano, M. Guillemot, P. Fabre, J. Courcambeck, C. Ansaldi, *et al.*, "Gns561, a new lysosomotropic small molecule, for the treatment of intrahepatic cholangiocarcinoma," *Investigational New Drugs*, vol. 37, pp. 1135–1145, 2019.

[54] C. Wang, H. Lv, W. Yang, T. Li, T. Fang, G. Lv, Q. Han, L. Dong, T. Jiang, B. Jiang, *et al.*, "Svct-2 determines the sensitivity to ascorbate-induced cell death in cholangiocarcinoma cell lines and patient derived xenografts," *Cancer Letters*, vol. 398, pp. 1–11, 2017.

[55] L. N. Boyd, G. J. Peters, G. Kazemier, and E. Giovannetti, "Nuc-1031 in biliary tract cancer: from bench to bedside and back?," *Cancer Chemotherapy and Pharmacology*, vol. 85, no. 6, pp. 1011–1014, 2020.

[56] Y. Wang, X. Ding, S. Wang, C. D. Moser, H. M. Shaleh, E. A. Mohamed, R. Chaiteerakij, L. K. Allotey, G. Chen, K. Miyabe, *et al.*, "Antitumor effect of fgfr inhibitors on a novel cholangiocarcinoma patient derived xenograft mouse model endogenously expressing an fgfr2-ccdc6 fusion protein," *Cancer letters*, vol. 380, no. 1, pp. 163–173, 2016.

[57] J. Wu, J. Sheng, H. Qin, M. Cui, Y. Yang, and X. Zhang, "The application progress of patient-derived tumor xenograft models after cholangiocarcinoma surgeries," *Frontiers in Oncology*, p. 2799, 2021.

[58] L. Pompili, M. Porru, C. Caruso, A. Biroccio, and C. Leonetti, "Patient-derived xenografts: a relevant preclinical model for drug development," *Journal of Experimental & Clinical Cancer Research*, vol. 35, no. 1, pp. 1–8, 2016.

[59] M. R. O'Dell, J. Li Huang, C. L. Whitney-Miller, V. Deshpande, P. Rothberg, V. Grose, R. M. Rossi, A. X. Zhu, H. Land, N. Bardeesy, *et al.*, "Krasg12d and p53 mutation cause primary intrahepatic cholangiocarcinomakras and p53 cooperate to cause intrahepatic cholangiocarcinoma," *Cancer research*, vol. 72, no. 6, pp. 1557–1567, 2012.

[60] H. Zhu, X. Jiang, X. Zhou, X. Dong, K. Xie, C. Yang, H. Jiang, X. Sun, and J. Lu, "Neuropilin-1 regulated by mir-320 contributes to the growth and metastasis of cholangiocarcinoma cells," *Liver International*, vol. 38, no. 1, pp. 125–135, 2018.

[61] L. Broutier, G. Mastrogiovanni, M. Verstegen, H. E. Francies, L. M. Gavarró, C. R. Bradshaw, G. E. Allen, R. Arnes-Benito, O. Sidorova, M. P. Gaspersz, *et al.*, "Human primary liver cancer–derived organoid cultures for disease modeling and drug screening," *Nature medicine*, vol. 23, no. 12, pp. 1424–1435, 2017.

[62] J. Drost and H. Clevers, "Organoids in cancer research," *Nature Reviews Cancer*, vol. 18, no. 7, pp. 407–418, 2018.

[63] D. Tuveson and H. Clevers, "Cancer modeling meets human organoid technology," *Science*, vol. 364, no. 6444, pp. 952–955, 2019.

[64] V. Veninga and E. E. Voest, "Tumor organoids: Opportunities and challenges to guide precision medicine," *Cancer Cell*, vol. 39, no. 9, pp. 1190–1201, 2021.

[65] J. Winkler, A. Abisoye-Ogunniyan, K. J. Metcalf, and Z. Werb, "Concepts of extracellular matrix remodelling in tumour progression and metastasis," *Nature communications*, vol. 11, no. 1, pp. 1–19, 2020.

[66] A. Malandrino, R. D. Kamm, and E. Moeendarbary, "In vitro modeling of mechanics in cancer metastasis," *ACS biomaterials science & engineering*, vol. 4, no. 2, pp. 294–301, 2018.

[67] M. T. Kozlowski, C. J. Crook, and H. T. Ku, "Towards organoid culture without matrigel," *Communications biology*, vol. 4, no. 1, pp. 1–15, 2021.

[68] E. A. Aisenbrey and W. L. Murphy, "Synthetic alternatives to matrigel," *Nature Reviews Materials*, vol. 5, no. 7, pp. 539–551, 2020.

[69] C. S. Hughes, L. M. Postovit, and G. A. Lajoie, "Matrigel: a complex protein mixture required for optimal growth of cell culture," *Proteomics*, vol. 10, no. 9, pp. 1886–1890, 2010.

[70] E. L. Baker, R. T. Bonnecaze, and M. H. Zaman, "Extracellular matrix stiffness and architecture govern intracellular rheology in cancer," *Biophysical journal*, vol. 97, no. 4, pp. 1013–1021, 2009.

[71] V. Rajagopal, W. R. Holmes, and P. V. S. Lee, "Computational modeling of single-cell mechanics and cytoskeletal mechanobiology," *Wiley Interdisciplinary Reviews: Systems Biology and Medicine*, vol. 10, no. 2, p. e1407, 2018.

[72] S. Ishihara and H. Haga, "Matrix stiffness contributes to cancer progression by regulating transcription factors," *Cancers*, vol. 14, no. 4, p. 1049, 2022.

[73] T. W. Gilbert, T. L. Sellaro, and S. F. Badylak, "Decellularization of tissues and organs," *Biomaterials*, vol. 27, no. 19, pp. 3675–3683, 2006.

[74] T. J. Keane, I. T. Swinehart, and S. F. Badylak, "Methods of tissue decellularization used for preparation of biologic scaffolds and in vivo relevance," *Methods*, vol. 84, pp. 25–34, 2015.

[75] D. K. Mishra and M. P. Kim, "Acellular and cellular lung model to study tumor metastasis," *JoVE (Journal of Visualized Experiments)*, no. 138, p. e58145, 2018.

[76] X. Tian, M. E. Werner, K. C. Roche, A. D. Hanson, H. P. Foote, S. K. Yu, S. B. Warner, J. A. Copp, H. Lara, E. L. Wauthier, *et al.*, "Organ-specific metastases obtained by culturing colorectal cancer cells on tissue-specific decellularized scaffolds," *Nature biomedical engineering*, vol. 2, no. 6, pp. 443–452, 2018.

[77] F. Sensi, E. D'Angelo, M. Piccoli, P. Pavan, F. Mastrotto, P. Caliceti, A. Biccari, D. Corallo, L. Urbani, M. Fassan, *et al.*, "Recellularized colorectal cancer patient-derived scaffolds as in vitro pre-clinical 3d model for drug screening," *Cancers*, vol. 12, no. 3, p. 681, 2020.

[78] D. Fecher, E. Hofmann, A. Buck, R. Bundschuh, S. Nietzer, G. Dandekar, T. Walles, H. Walles, K. Lückerath, and M. Steinke, "Human organotypic lung tumor models: suitable for preclinical 18f-fdg pet-imaging," *PloS one*, vol. 11, no. 8, p. e0160282, 2016.

[79] G. S. van Tienderen, O. Rosmark, R. Lieshout, J. Willemse, F. de Weijer, L. E. Rendin, G. Westergren-Thorsson, M. Doukas, B. G. Koerkamp, M. E. van Royen, *et al.*, "Extracellular matrix drives tumor organoids toward desmoplastic matrix deposition and mesenchymal transition," *Acta Biomaterialia*, 2022.

[80] O. Chaudhuri, J. Cooper-White, P. A. Janmey, D. J. Mooney, and V. B. Shenoy, "Effects of extracellular matrix viscoelasticity on cellular behaviour," *Nature*, vol. 584, no. 7822, pp. 535–546, 2020.

[81] N. K. Altorki, G. J. Markowitz, D. Gao, J. L. Port, A. Saxena, B. Stiles, T. McGraw, and V. Mittal, "The lung microenvironment: an important regulator of tumour growth and metastasis," *Nature Reviews Cancer*, vol. 19, no. 1, pp. 9–31, 2019.

[82] J. R. Guarin, J. P. Fatherree, and M. J. Oudin, "Chemotherapy treatment induces pro-invasive changes in liver ecm composition," *Matrix Biology*, vol. 112, pp. 20–38, 2022.

[83] G. S. van Tienderen, J. Conboy, I. Muntz, J. Willemse, J. Tieleman, K. Monfils, I. J. Schurink, J. A. Demmers, M. Doukas, G. H. Koenderink, *et al.*, "Tumor decellularization reveals proteomic and mechanical characteristics of the extracellular matrix of primary liver cancer," *Biomaterials Advances*, p. 213289, 2023.

[84] S.-V. Kontomaris, "The hertz model in afm nanoindentation experiments: applications in biological samples and biomaterials," *Micro and Nanosystems*, vol. 10, no. 1, pp. 11–22, 2018.

[85] K. Khanafer, M. Schlicht, and R. Berguer, "How should we measure and report elasticity in aortic tissue?," *European Journal of Vascular and Endovascular Surgery*, vol. 45, no. 4, pp. 332–339, 2013.

[86] J. Vandesompele, K. De Preter, F. Pattyn, B. Poppe, N. Van Roy, A. De Paepe, and F. Speleman, "Accurate normalization of real-time quantitative rt-pcr data by geometric averaging of multiple internal control genes," *Genome biology*, vol. 3, no. 7, pp. 1–12, 2002.

[87] M. A. Wallig, B. Bolon, W. M. Haschek, and C. G. Rousseaux, *Fundamentals of toxicologic pathology.* Academic press, 2017.

[88] H.-J. Lin, W. Wang, Y.-Y. Huang, W.-T. Liao, T.-Y. Lin, S.-Y. Lin, and D.-Z. Liu, "Decellularized lymph node scaffolding as a carrier for dendritic cells to induce anti-tumor immunity," *Pharmaceutics*, vol. 11, no. 11, p. 553, 2019.

[89] E. García-Gareta, Y. Abduldaiem, P. Sawadkar, C. Kyriakidis, F. Lali, and K. V. Greco, "Decellularised scaffolds: just a framework? current knowledge and future directions," *Journal of Tissue Engineering*, vol. 11, p. 2041731420942903, 2020.

[90] N. Poornejad, L. B. Schaumann, E. M. Buckmiller, N. Momtahan, J. R. Gassman, H. H. Ma, B. L. Roeder, P. R. Reynolds, and A. D. Cook, "The impact of decellularization agents on renal tissue extracellular matrix," *Journal of biomaterials applications*, vol. 31, no. 4, pp. 521–533, 2016.

[91] P. M. Crapo, T. W. Gilbert, and S. F. Badylak, "An overview of tissue and whole organ decellularization processes," *Biomaterials*, vol. 32, no. 12, pp. 3233–3243, 2011.

[92] A. Gilpin and Y. Yang, "Decellularization strategies for regenerative medicine: from processing techniques to applications," *BioMed research international*, vol. 2017, 2017.

[93] R. Annoni, T. Lanças, R. Y. Tanigawa, M. de Medeiros Matsushita, S. de Morais Fernezlian, A. Bruno, L. F. F. da Silva, P. J. Roughley, S. Battaglia, M. Dolhnikoff, *et al.*, "Extracellular matrix composition in copd," *European Respiratory Journal*, vol. 40, no. 6, pp. 1362–1373, 2012.

[94] B. Suki and J. H. Bates, "Extracellular matrix mechanics in lung parenchymal diseases," *Respiratory physiology & neurobiology*, vol. 163, no. 1-3, pp. 33–43, 2008.

[95] S. E. Dunsmore, "Treatment of copd: a matrix perspective," *International journal of chronic obstructive pulmonary disease*, vol. 3, no. 1, p. 113, 2008.

[96] E. Bateman, M. Turner-Warwick, and B. Adelmann-Grill, "Immunohistochemical study of collagen types in human foetal lung and fibrotic lung disease.," *Thorax*, vol. 36, no. 9, pp. 645–653, 1981.

[97] T. Harju, V. L. Kinnula, P. Pääkkö, K. Salmenkivi, J. Risteli, and R. Kaarteenaho, "Variability in the precursor proteins of collagen i and iii in different stages of copd," *Respiratory research*, vol. 11, no. 1, pp. 1–10, 2010.

[98] C. L. Willard-Mack, "Normal structure, function, and histology of lymph nodes," *Toxicologic pathology*, vol. 34, no. 5, pp. 409–424, 2006.

[99] R. E. Moe, "Fine structure of the reticulum and sinuses of lymph nodes," *American Journal of Anatomy*, vol. 112, no. 3, pp. 311–335, 1963.

[100] J. Wei, M. Hu, K. Huang, S. Lin, and H. Du, "Roles of proteoglycans and glycosaminoglycans in cancer development and progression," *International journal of molecular sciences*, vol. 21, no. 17, p. 5983, 2020.

[101] D. Vitale, S. Kumar Katakam, B. Greve, B. Jang, E.-S. Oh, L. Alaniz, and M. Götte, "Proteoglycans and glycosaminoglycans as regulators of cancer stem cell function and therapeutic resistance," *The FEBS Journal*, vol. 286, no. 15, pp. 2870–2882, 2019.

[102] P. Fratzl, *Collagen: structure and mechanics, an introduction.* Springer, 2008.

[103] Y. Saito, T. Muramatsu, Y. Kanai, H. Ojima, A. Sukeda, N. Hiraoka, E. Arai, Y. Sugiyama, J. Matsuzaki, R. Uchida, *et al.*, "Establishment of patient-derived organoids and drug screening for biliary tract carcinoma," *Cell reports*, vol. 27, no. 4, pp. 1265–1276, 2019.

[104] S. Usman, N. H. Waseem, T. K. N. Nguyen, S. Mohsin, A. Jamal, M.-T. Teh, and A. Waseem, "Vimentin is at the heart of epithelial mesenchymal transition (emt) mediated metastasis," *Cancers*, vol. 13, no. 19, p. 4985, 2021.

[105] N. Zhai, J. Liu, P. Xu, B. Liu, Y. Fan, and C. Lv, "Pulmonary metastasis of distal cholangiocarcinoma with multiple cavities in bilateral lungs: A case report," *Thoracic Cancer*, vol. 11, no. 10, pp. 2998–3000, 2020.

[106] L. Yang, P. Shi, G. Zhao, J. Xu, W. Peng, J. Zhang, G. Zhang, X. Wang, Z. Dong, F. Chen, *et al.*, "Targeting cancer stem cell pathways for cancer therapy," *Signal transduction and targeted therapy*, vol. 5, no. 1, pp. 1–35, 2020.

[107] P. M. Glumac and A. M. LeBeau, "The role of cd133 in cancer: a concise review," *Clinical and translational medicine*, vol. 7, no. 1, pp. 1–14, 2018.

[108] P. Chu, E. Wu, and L. M. Weiss, "Cytokeratin 7 and cytokeratin 20 expression in epithelial neoplasms: a survey of 435 cases," *Modern Pathology*, vol. 13, no. 9, pp. 962–972, 2000.

[109] Y. I. Petrova, L. Schecterson, and B. M. Gumbiner, "Roles for e-cadherin cell surface regulation in cancer," *Molecular biology of the cell*, vol. 27, no. 21, pp. 3233–3244, 2016.

[110] T.-Y. Na, L. Schecterson, A. M. Mendonsa, and B. M. Gumbiner, "The functional activity of e-cadherin controls tumor cell metastasis at multiple steps," *Proceedings of the National Academy of Sciences*, vol. 117, no. 11, pp. 5931–5937, 2020.

[111] A. Techasen, W. Loilome, N. Namwat, N. Khuntikeo, A. Puapairoj, P. Jearanaikoon, H. Saya, and P. Yongvanit, "Loss of e-cadherin promotes migration and invasion of cholangiocarcinoma cells and serves as a potential marker of metastasis," *Tumor Biology*, vol. 35, no. 9, pp. 8645–8652, 2014.

[112] G. Carpino, D. Overi, F. Melandro, A. Grimaldi, V. Cardinale, S. Di Matteo, G. Mennini, M. Rossi, D. Alvaro, V. Barnaba, *et al.*, "Matrisome analysis of intrahepatic cholangiocarcinoma unveils a peculiar cancer-associated extracellular matrix structure," *Clinical proteomics*, vol. 16, no. 1, pp. 1–12, 2019.

[113] H. Hamidi and J. Ivaska, "Every step of the way: integrins in cancer progression and metastasis," *Nature Reviews Cancer*, vol. 18, no. 9, pp. 533–548, 2018.

[114] J. A. Eble and S. Niland, "The extracellular matrix in tumor progression and metastasis," *Clinical & experimental metastasis*, vol. 36, no. 3, pp. 171–198, 2019.

[115] L. Gillot, A. Lebeau, L. Baudin, C. Pottier, T. Louis, T. Durré, R. Longuespée, G. Mazzucchelli, C. Nizet, S. Blacher, *et al.*, "Periostin in lymph node pre-metastatic niches governs lymphatic endothelial cell functions and metastatic colonization," *Cellular and Molecular Life Sciences*, vol. 79, no. 6, p. 295, 2022.

[116] B. A. Aguado, J. R. Caffe, D. Nanavati, S. S. Rao, G. G. Bushnell, S. M. Azarin, and L. D. Shea, "Extracellular matrix mediators of metastatic cell colonization characterized using scaffold mimics of the pre-metastatic niche," *Acta biomaterialia*, vol. 33, pp. 13–24, 2016.

[117] H. Großkopf, S. Vogel, C. D. Müller, S. Köhling, J.-N. Dürig, S. Möller, M. Schnabelrauch, J. Rademann, U. Hempel, M. von Bergen, *et al.*, "Identification of intracellular glycosaminoglycan-interacting proteins by affinity purification mass spectrometry," *Biological Chemistry*, vol. 402, no. 11, pp. 1427–1440, 2021.

[118] B. Emon, J. Bauer, Y. Jain, B. Jung, and T. Saif, "Biophysics of tumor microenvironment and cancer metastasis-a mini review," *Computational and Structural Biotechnology Journal*, vol. 16, pp. 279–287, 2018.

[119] F. Spill, D. S. Reynolds, R. D. Kamm, and M. H. Zaman, "Impact of the physical microenvironment on tumor progression and metastasis," *Current opinion in biotechnology*, vol. 40, pp. 41–48, 2016.

[120] E. Melo, E. Garreta, T. Luque, J. Cortiella, J. Nichols, D. Navajas, and R. Farré, "Effects of the decellularization method on the local stiffness of acellular lungs," *Tissue Engineering Part C: Methods*, vol. 20, no. 5, pp. 412–422, 2014.

[121] F. P. Assen, J. Abe, M. Hons, R. Hauschild, S. Shamipour, W. A. Kaufmann, T. Costanzo, G. Krens, M. Brown, B. Ludewig, *et al.*, "Multitier mechanics control stromal adaptations in the swelling lymph node," *Nature Immunology*, pp. 1–10, 2022.

[122] M. Matsuoka, M. Okamoto, T. Soma, I. Yokota, R. Arai, T. Onodera, E. Kondo, N. Iwasaki, and H. Hiraga, "Impact of smoking history on pulmonary metastasis-free survival in patients with soft-tissue sarcoma," *Cancer Diagnosis & Prognosis*, vol. 1, no. 2, p. 89, 2021.

[123] J. Guo, S. Zhang, H. Li, M. O. O. Hassan, T. Lu, J. Zhao, and L. Zhang, "Lung metastases in newly diagnosed esophageal cancer: a population-based study," *Frontiers in oncology*, vol. 11, p. 603953, 2021.

[124] A. Tyagi, S. Sharma, K. Wu, S.-Y. Wu, F. Xing, Y. Liu, D. Zhao, R. P. Deshpande, R. B. D'Agostino, and K. Watabe, "Nicotine promotes breast cancer metastasis by stimulating n2 neutrophils and generating pre-metastatic niche in lung," *Nature communications*, vol. 12, no. 1, pp. 1–18, 2021.

[125] M. Yahagi, M. Tsuruta, H. Hasegawa, K. Okabayashi, N. Toyoda, N. Iwama, S. Morita, and Y. Kitagawa, "Smoking is a risk factor for pulmonary metastasis in colorectal cancer," *Colorectal Disease*, vol. 19, no. 9, pp. O322–O328, 2017.

[126] T. Yoshizawa, T. Uehara, M. Iwaya, S. Asaka, S. Kobayashi, T. Nakajima, Y. Kinugawa, T. Nagaya, M. Kamakura, A. Shimizu, *et al.*, "Correlation of lgr5 expression and clinicopathological features in intrahepatic cholangiocarcinoma," *Pathology-Research and Practice*, vol. 232, p. 153832, 2022.

[127] X. Cai, J. Li, X. Yuan, J. Xiao, S. Dooley, X. Wan, H. Weng, and L. Lu, "Cd133 expression in cancer cells predicts poor prognosis of non-mucin producing intrahepatic cholangiocarcinoma," *Journal of Translational Medicine*, vol. 16, no. 1, pp. 1–7, 2018.

[128] M. Narciso, A. Ulldemolins, C. Júnior, J. Otero, D. Navajas, R. Farre, N. Gavara, and I. Almendros, "Novel decellularization method for tissue slices," *Frontiers in bioengineering and biotechnology*, p. 271, 2022.

[129] D. A. Cuzzone, N. J. Albano, S. Z. Aschen, S. Ghanta, and B. J. Mehrara, "Decellularized lymph nodes as scaffolds for tissue engineered lymph nodes," *Lymphatic research and biology*, vol. 13, no. 3, pp. 186–194, 2015.

[130] J. D. O'Neill, R. Anfang, A. Anandappa, J. Costa, J. Javidfar, H. M. Wobma, G. Singh, D. O. Freytes, M. D. Bacchetta, J. R. Sonett, *et al.*, "Decellularization of human and porcine lung tissues for pulmonary tissue engineering," *The Annals of thoracic surgery*, vol. 96, no. 3, pp. 1046–1056, 2013.

[131] U. Mendibil, R. Ruiz-Hernandez, S. Retegi-Carrion, N. Garcia-Urquia, B. Olalde-Graells, and A. Abarrategi, "Tissue-specific decellularization methods: rationale and strategies to achieve regenerative compounds," *International journal of molecular sciences*, vol. 21, no. 15, p. 5447, 2020.

[132] L. Liu, B. Stephens, M. Bergman, A. May, and T. Chiang, "Role of collagen in airway mechanics," *Bioengineering*, vol. 8, no. 1, p. 13, 2021.

[133] D. Moffat, K. Ye, and S. Jin, "Decellularization for the retention of tissue niches," *Journal of Tissue Engineering*, vol. 13, p. 20417314221101151, 2022.

[134] E. Gentilin, E. D'Angelo, M. Agostini, and L. Astolfi, "Decellularized normal and cancer tissues as tools for cancer research," *Cancer Gene Therapy*, pp. 1–10, 2021.

[135] E. K. U. Larsen, N. B. Larsen, K. Almdal, E. Larsen, N. Larsen, and K. Almdal, “Multimaterial hydrogel with widely tunable elasticity by selective photopolymerization of peg diacrylate and epoxy monomers,” *Journal of Polymer Science Part B: Polymer Physics*, vol. 54, no. 13, pp. 1195–1201, 2016.

[136] N. Gjorevski, M. Nikolaev, T. Brown, O. Mitrofanova, N. Brandenberg, F. DelRio, F. Yavitt, P. Liberali, K. Anseth, and M. Lutolf, “Tissue geometry drives deterministic organoid patterning,” *Science*, vol. 375, no. 6576, p. eaaw9021, 2022.

[137] H.-H. Liu, Y. Xu, C.-J. Li, S.-J. Hsu, X.-H. Lin, R. Zhang, J. Chen, J. Chen, D.-M. Gao, J.-F. Cui, *et al.*, “An scd1-dependent mechanoresponsive pathway promotes hcc invasion and metastasis through lipid metabolic reprogramming,” *Molecular Therapy*, 2022.

[138] J. Willemse, G. van Tienderen, E. van Hengel, I. Schurink, D. van der Ven, Y. Kan, P. de Ruiter, O. Rosmark, K. Schneeberger, B. van der Eerden, *et al.*, “Hydrogels derived from decellularized liver tissue support the growth and differentiation of cholangiocyte organoids,” *Biomaterials*, vol. 284, p. 121473, 2022.

[139] M. d’Angelo, E. Benedetti, M. G. Tupone, M. Catanesi, V. Castelli, A. Antonosante, and A. Cimini, “The role of stiffness in cell reprogramming: a potential role for biomaterials in inducing tissue regeneration,” *Cells*, vol. 8, no. 9, p. 1036, 2019.

[140] L. Hof, T. Moreth, M. Koch, T. Liebisch, M. Kurtz, J. Tarnick, S. M. Lissek, M. Verstegen, L. J. van der Laan, M. Huch, *et al.*, “Long-term live imaging and multiscale analysis identify heterogeneity and core principles of epithelial organoid morphogenesis,” *BMC biology*, vol. 19, no. 1, pp. 1–22, 2021.

[141] Y. Wang, D. Wu, G. Wu, J. Wu, S. Lu, J. Lo, Y. He, C. Zhao, X. Zhao, H. Zhang, *et al.*, “Metastasis-on-a-chip mimicking the progression of kidney cancer in the liver for predicting treatment efficacy,” *Theranostics*, vol. 10, no. 1, p. 300, 2020.

[142] O. Braissant, M. Astasov-Frauenhoffer, T. Waltimo, and G. Bonkat, “A review of methods to determine viability, vitality, and metabolic rates in microbiology,” *Frontiers in Microbiology*, vol. 11, p. 547458, 2020.

[143] H. Kim, H. Chung, J. Kim, D.-H. Choi, Y. Shin, Y. G. Kang, B.-M. Kim, S.-U. Seo, S. Chung, and S. H. Seok, “Macrophages-triggered sequential remodeling of endothelium-interstitial matrix to form pre-metastatic niche in microfluidic tumor microenvironment,” *Advanced Science*, vol. 6, no. 11, p. 1900195, 2019.

[144] B. A. Aguado, G. G. Bushnell, S. S. Rao, J. S. Jeruss, and L. D. Shea, “Engineering the pre-metastatic niche,” *Nature biomedical engineering*, vol. 1, no. 6, pp. 1–12, 2017.

[145] A. Yokoi and T. Ochiya, “Exosomes and extracellular vesicles: Rethinking the essential values in cancer biology,” in *Seminars in Cancer Biology*, vol. 74, pp. 79–91, Elsevier, 2021.

[146] X. Yang, Y. Zhang, Y. Zhang, S. Zhang, L. Qiu, Z. Zhuang, M. Wei, X. Deng, Z. Wang, and J. Han, “The key role of exosomes on the pre-metastatic niche formation in tumors,” *Frontiers in molecular biosciences*, vol. 8, p. 703640, 2021.

[147] G. Zhou, R. Lieshout, G. S. van Tienderen, V. de Ruiter, M. E. van Royen, P. P. Boor, L. Magré, J. Desai, K. Köten, Y. Y. Kan, *et al.*, “Modelling immune cytotoxicity for cholangiocarcinoma with tumour-derived organoids and effector t cells,” *British Journal of Cancer*, pp. 1–12, 2022.

[148] J. J. Sleeboom, H. Eslami Amirabadi, P. Nair, C. M. Sahlgren, and J. M. Den Toonder, “Metastasis in context: modeling the tumor microenvironment with cancer-on-a-chip approaches,” *Disease models & mechanisms*, vol. 11, no. 3, p. dmm033100, 2018.

[149] X. Zhang, M. Karim, M. M. Hasan, J. Hooper, R. Wahab, S. Roy, and T. A. Al-Hilal, “Cancer-on-a-chip: Models for studying metastasis,” *Cancers*, vol. 14, no. 3, p. 648, 2022.

[150] M. A. Morsink, N. G. Willemen, J. Leijten, R. Bansal, and S. R. Shin, “Immune organs and immune cells on a chip: an overview of biomedical applications,” *Micromachines*, vol. 11, no. 9, p. 849, 2020.

[151] W. M. S. Russell and R. L. Burch, *The principles of humane experimental technique.* Methuen, 1959.

[152] I. Jorba, G. Beltrán, B. Falcones, B. Suki, R. Farré, J. M. García-Aznar, and D. Navajas, "Nonlinear elasticity of the lung extracellular microenvironment is regulated by macroscale tissue strain," *Acta biomaterialia*, vol. 92, pp. 265–276, 2019.

[153] C. Júnior, M. Narciso, E. Marhuenda, I. Almendros, R. Farré, D. Navajas, J. Otero, and N. Gavara, "Baseline stiffness modulates the non-linear response to stretch of the extracellular matrix in pulmonary fibrosis," *International Journal of Molecular Sciences*, vol. 22, no. 23, p. 12928, 2021.

[154] R. A. Pouliot, P. A. Link, N. S. Mikhaiel, M. B. Schneck, M. S. Valentine, F. J. Kamga Gninzeko, J. A. Herbert, M. Sakagami, and R. L. Heise, "Development and characterization of a naturally derived lung extracellular matrix hydrogel," *Journal of biomedical materials research Part A*, vol. 104, no. 8, pp. 1922–1935, 2016.

[155] R. H. J. de Hilster, P. K. Sharma, M. R. Jonker, E. S. White, E. A. Gercama, M. Roobeek, W. Timens, M. C. Harmsen, M. N. Hylkema, and J. K. Burgess, "Human lung extracellular matrix hydrogels resemble the stiffness and viscoelasticity of native lung tissue," *American Journal of Physiology-Lung Cellular and Molecular Physiology*, vol. 318, no. 4, pp. L698–L704, 2020.

[156] T. H. Petersen, E. A. Calle, M. B. Colehour, and L. E. Niklason, "Matrix composition and mechanics of decellularized lung scaffolds," *Cells Tissues Organs*, vol. 195, no. 3, pp. 222–231, 2012.

[157] Y. S. Choi, E. Jeong, J. S. Lee, S. K. Kim, S.-H. Jo, Y.-G. Kim, H.-J. Sung, S.-W. Cho, and Y. Jin, "Immunomodulatory scaffolds derived from lymph node extracellular matrices," *ACS applied materials & interfaces*, vol. 13, no. 12, pp. 14037–14049, 2021.

[158] A. J. Booth, R. Hadley, A. M. Cornett, A. A. Dreffs, S. A. Matthes, J. L. Tsui, K. Weiss, J. C. Horowitz, V. F. Fiore, T. H. Barker, *et al.*, "Acellular normal and fibrotic human lung matrices as a culture system for in vitro investigation," *American journal of respiratory and critical care medicine*, vol. 186, no. 9, pp. 866–876, 2012.

Supplementary Materials and Methods

Sample procurement

The collection of the tissue and initiation of the organoids was already done by the lab staff of the Erasmus MC. I received the organoids in a 24-well plate that were already passaged 144 times.

Component	Concentration	Brand
AdvDMEM12+++	82.6%	Gibco
N2	1%	Gibco
B27	2%	Gibco
Gastrin I	10 nM	Sigma
FGF10	100 ng/ml	Peprotech
HGF	25 ng/ml	Peprotech
EGF	50 ng/ml	Peprotech
A83.01(Ti)	5 μM	Tocris
Nicotinamide	10 mM	Sigma
Forskolin	10 μM	Tocris
Acetylcystein	1 mM	Sigma
R-SPondin CM	10%	Conditioned medium

Table S1: **EM components, concentrations and brands.**

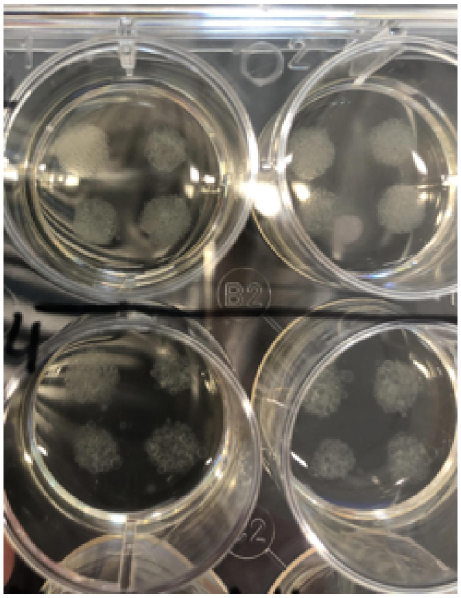

Figure S1: **CCAO in BME domes cultured in a 12-well plate.**

Decellularization

Lymph node	Human donor type[1]	M/F	Age	BMI	Smoking	Pack years[2]
Lymph node1	DCD	M	56	25	No	0
Lymph node2	DBD	F	57	28	No	0
Lymph node3	DBD	F	55	15	Yes	50
Lymph node4	DCD	M	13	16	No	0
Lymph node5	DBD	F	44	25	Yes	12
Lymph node6	DBD	M	82	27	No	0
Lymph node7	DBD	M	55	23	Yes	5
Lymph node8	DBD	M	50	26	Yes	15
Lymph node9	DBD	F	74	22	No	0
Lymph node10	DBD	M	58	21	No	0
Lymph node11	DBD	F	63	21	Yes	13
Lymph node12	DBD	M	31	31	Yes	1
Lymph node13	DBD	F	58	21	No	0
Lymph node14	DCD	M	51	24	No	0
Lymph node15	DBD	F	31	26	No	0
Lymph node16	DBD	M	47	24	No	0
Lymph node17	DCD	F	55	26	No	0

Table S2: **Information lymph node donors.** Human donor type[1]: DCD = donation after circulatory dead, DBD = donation after brain dead. Pack years[2]: a pack year is defined as 20 cigarettes smoked every day for one year.

Analysis	Lymph nodes used
DNA content	Lymph node1-17
Collagen assay	Lymph node6,7,8,17 (T=0); dNECM1,2,8,15 (T=decell)
sGAG assay	Lymph node4,8,9,10,17 (T=0); dNECM2,3,4,13,16 (T=decell)
Nanoindentation	dNECM1, dNECM2, dNECM3
Rheology	dNECM2, dNECM10, dNECM16
Recellularization trial	dNECM5

Table S3: **Lymph nodes used per analysis.** Numbers corresponds with patient ID in excel file 'Lymph nodes.MvB'.

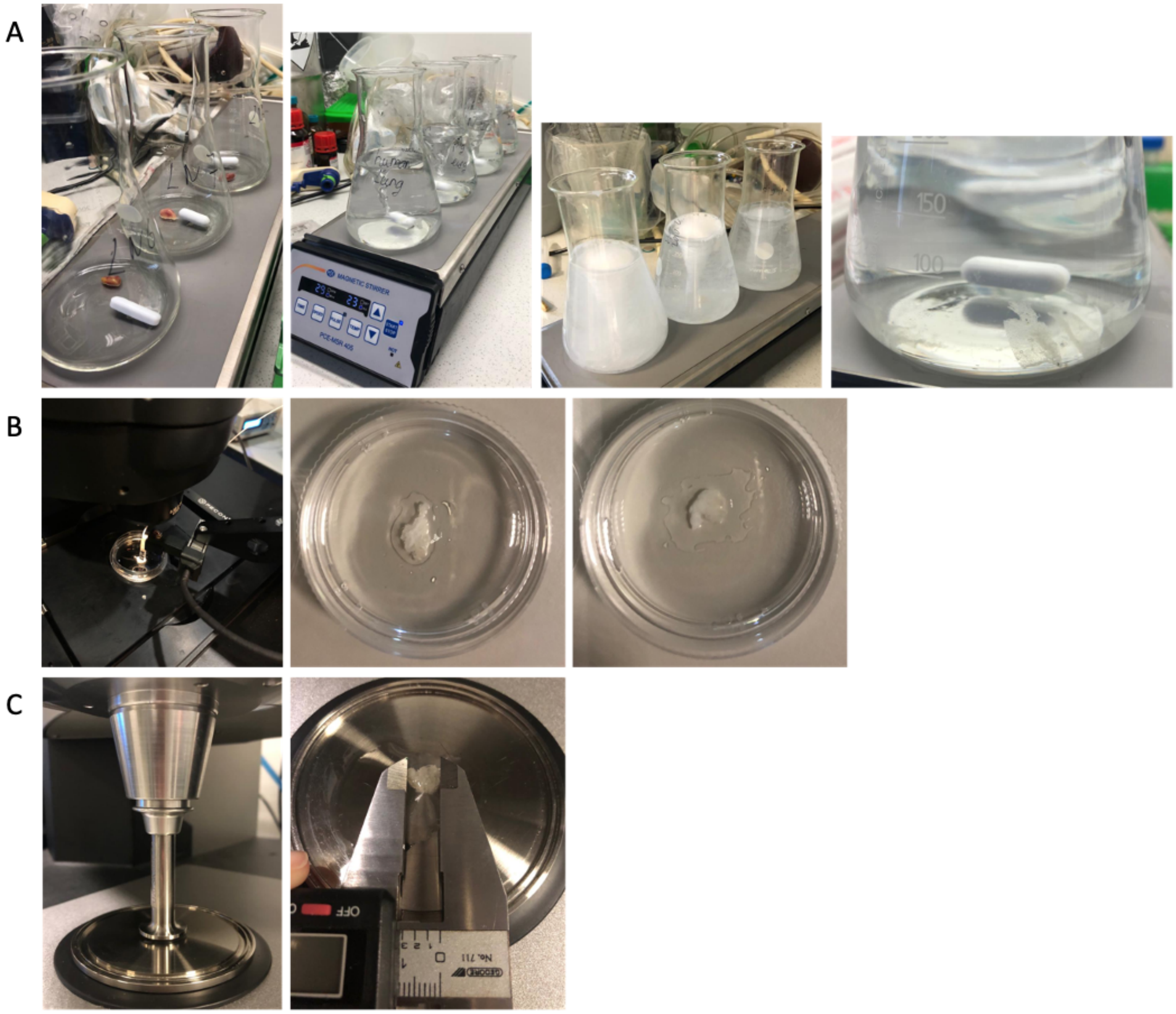

Figure S2: **Decellularization process and mechanical characterization experimental set-up. A)** Decellularization process for lung tissue and lymph nodes in an Erlenmeyer flask on a multi-position magnetic stirrer. **B)** Nanoindentation experimental set-up (left) and glued decellularized lung (middle) and lymph node (right) inside a 35 mm petri dish. **C)** Rheology experimental set-up (left) and sample width measurement of a decellularized lymph node (right).

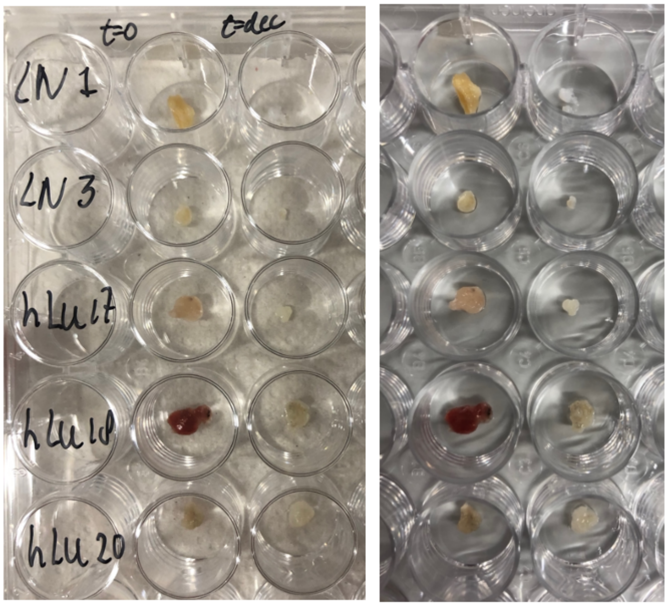

Figure S3: **Biopsies and decellularized lung and lymph nodes after fixation in 4% PFA and before the addition of 2% agarose and paraffin embedding.** hLu17, hLu18, hLu19 = Lung1, Lung2, Lung3.

Recellularization

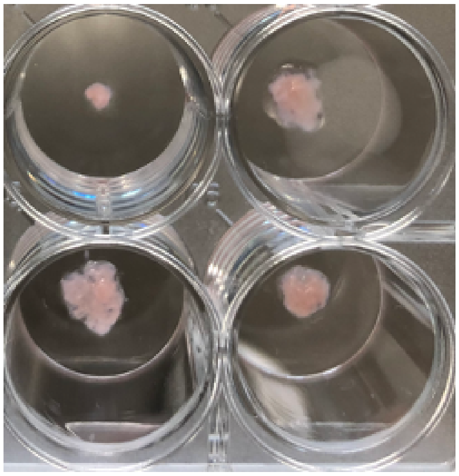

Figure S4: **Recellularization.** Recellularized dLECMs in 24-well suspension cell culture plate, demonstrating the drop of 5 μl cell-EM mixture onto the with AdvDMEM washed dLECM.

Genes	**Forward primer sequence 5' to 3'**	**Reverse primer sequence 5' to 3'**
CD133	CCTGGGGCTGCTGTTTATTA	ATCACCAACAGGGAGATTGC
Collagen A1	CCCAGGTCCCCCTGGAAAGA	CCCGGCAGCACCAGTAGC
Collagen A3	TACCAAGGACCCCCTGGTGAA	GGTCGTCCGGGTCTACCTGAT
E-cadherin	CTGGACAGGGAGGATTTTGA	ACCTGAGGCTTTGGATTCCT
Fibronectin	TGCACATGCTTTGGAGGCCA	GCATGAAGCACTCAATTGGGCA
GAPDH	CTTTTGCGTCGCCAGCCGAG	CCAGGCGCCCAATACGACCA
HPRT	ACCAGTCAACAGGGGACATAA	CTTCGTGGGGTCCTTTTCACC
Integrin A5	AGGGTCGGGGGCTTCAACTTA	GAGCGGCAGGGTGCATACTC
Integrin B1	GGACGCCGCGCGGAAAAGAT	CACCCACAATTTGGCCCTGCT
Ki67	CTACGGATTATACCTGGCCTTCC	AGGAAGCTGGATACGGATGTCA
KRT7	GGGGACGACCTCCGGAATAC	CTTGGCACGCTGGTTCTTGA
LGR5	GTCAGCTGCTCCCGAATCCC	TGAAACAGCTTGGGGGCACA
MUC1	AGAGAAGTTCAGTGCCCAGC	TGACATCCTGTCCCTGAGTG
Vimentin	CGGGAGAAATTGCAGGAGG	TGCTGTTCCTGAATCTGAGC

Table S4: **Primers**

Supplementary Results

Decellularization

Transparent dLECM slices stuck together (Fig. 5C, S5E). Whether lymph nodes were entirely intact or disintegrated after decellularization varied between lymph nodes (Fig. S5C).

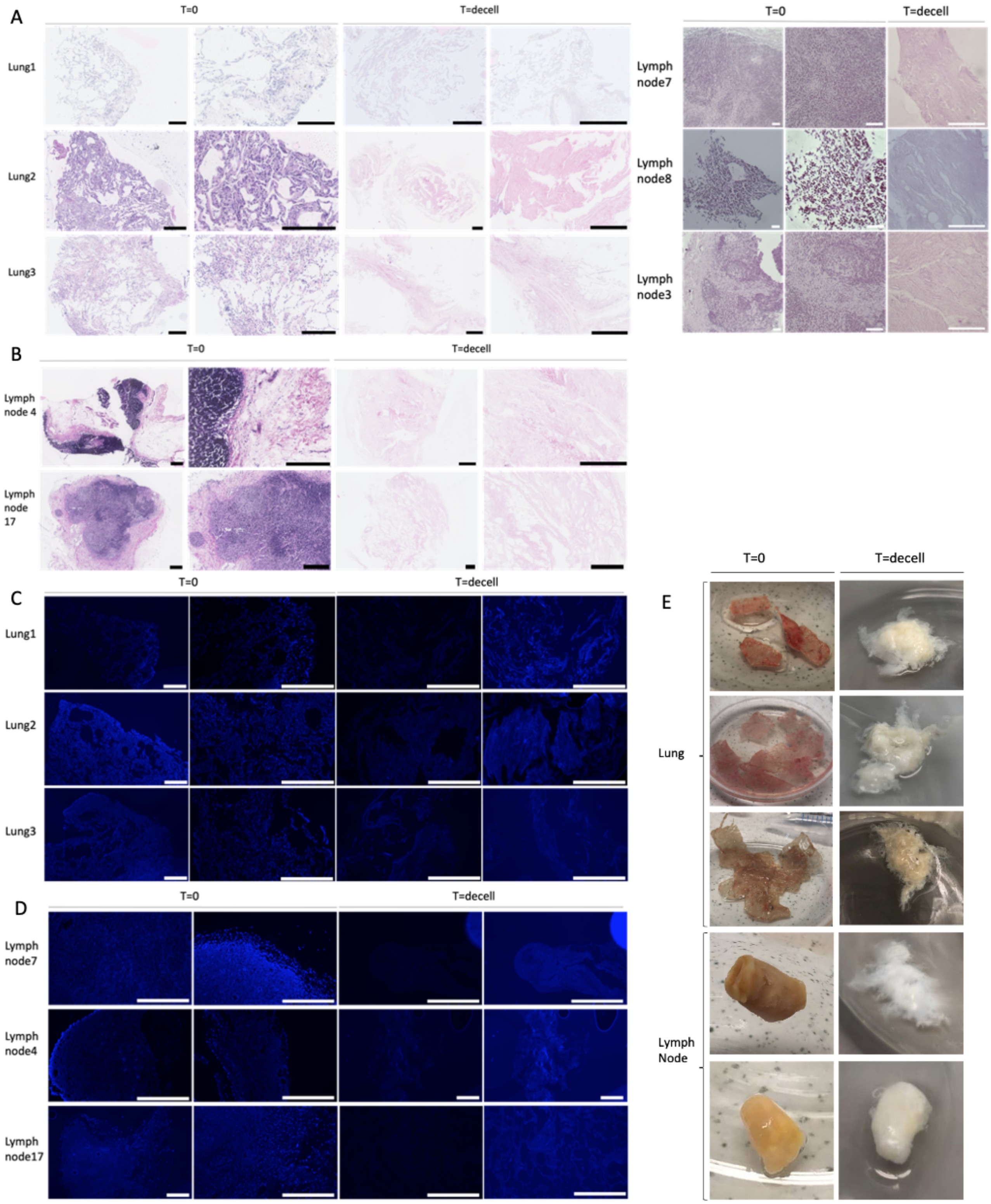

Figure S5: **Additional confirmation of successful dLECM and dNECM. A, B)** H&E staining of lung (n=3) and lymph nodes (n=5) before (T=0) and after (T=decell) decellularization showed efficient removal of cells from the scaffold and maintenance of ECM structure. Black scale bars for Lung1, Lung2, Lung3, LN1, LN27 indicate 250 μm, white scale bars for LN6, LN7, LN12 indicate 100 μm. **C, D)** DAPI staining of lung (n=3) and lymph nodes (n=3) before and after decellularization confirmed the removal of nuclear material from the scaffold. The image brightness was increased in the last column to make the remaining scaffold visible. Scale bars indicate 400 μm. **E)** Lung slices of 400 μm and entire lymph nodes of 1 cm before and after decellularization demonstrate the removal of cells and maintenance of ECM structure by its transparent appearance.

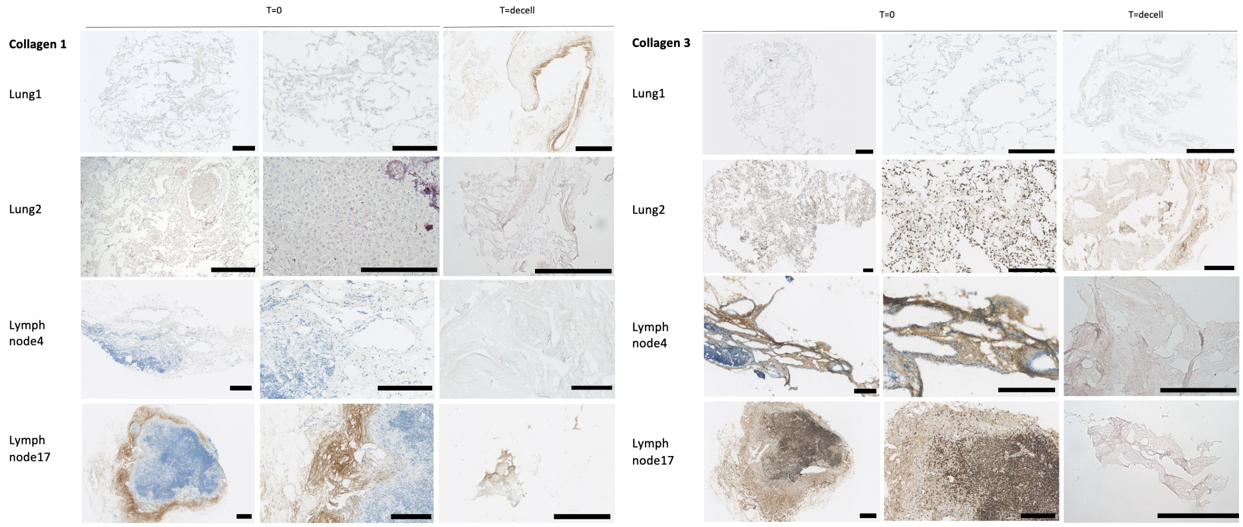

(a) Collagen A1

(b) Collagen A3

Figure S6: **Additional images of the preservation of ECM compound collagen type 1 (left) and type 3 (right) of before (T=0) and after (T=decell) decellularization for lung (n=2) and lymph nodes (n=2)**

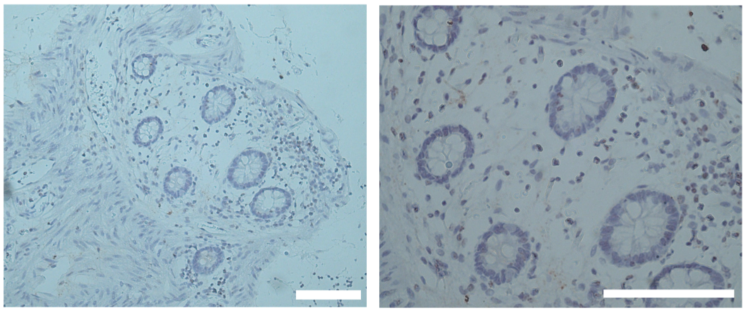

Figure S7: **Collagen type 3 staining of lung shows the bronchiole** (purple circles with cells). Scale bars indicate 100 μm.

Tissue type	Tissue Thickness	Method	Young's Modulus	Reference
Rat parenchymal strips (dLECM)	-	Uniaxial tensile testing	0.38± 0.07 kPa	[152]
Rat right upper lobe (dLECM)	20 μm	Tensile test	0.33-1.93 kPa	[153]
Porcine (dLECM hydrogel)	100 μl	Rheology	15-60 Pa	[154]
Human (dLECM hydrogel)	-	Stress relaxation testing	1.1± 0.2 kPa	[155]
Rat (dLECM)	-	Ultimate tensile strength	22.3± 1.8 kPa	[156]
Porcine (dNECM hydrogel)	5 mg/mL	Frequency sweep	93.09 Pa	[157]

Table S5: **Macroscopic properties of decellularized lung (hydrogel) and lymph node hydrogel.**

Tissue type	**Tissue Thickness**	**Method**	**Young's Modulus**	**Reference**
Human (dLECM)	1000 μm	AFM	1.6± 0.08 kPa	[158]
Rat parenchymal slices (dLECM)	16.8 μm	AFM	7.9± 0.7 kPa	[152]
Rat alveolar septum (dLECM)	-	AFM	15 kPa	[120]
Rat tunica intima (dLECM)	-	AFM	60 kPa	[120]
Rat (dLECM)	20 μm	AFM	1.3-7.1 kPa	[153]
Mice and Rat (dLECM)	20 μm	AFM	263.0± 29.9 Pa	[128]
Commercial BME	-	Nanoindentation	399± 114 Pa	[138]

Table S6: **Microscopic properties of decellularized lung and BME.**

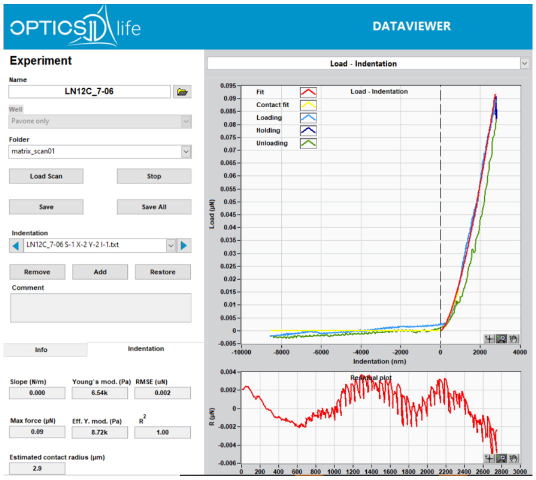

Name: LN12C_7-06
Well: Pavone only
Folder: matrix_scan01
Indentation: LN12C_7-06 S-1 X-2 Y-2 I-1.txt
Comment:
Slope (N/m): 0.000
Young`s mod. (Pa): 6.54k
RMSE (uN): 0.002
Max force (µN): 0.09
Eff. Y. mod. (Pa): 8.72k
R^2: 1.00
Estimated contact radius (µm): 2.9

Figure S8: **Representative graph obtained during nanoindentation using Optics 11 life software.** Viscoelastic behavior is visible (space between loading and unloading curve).

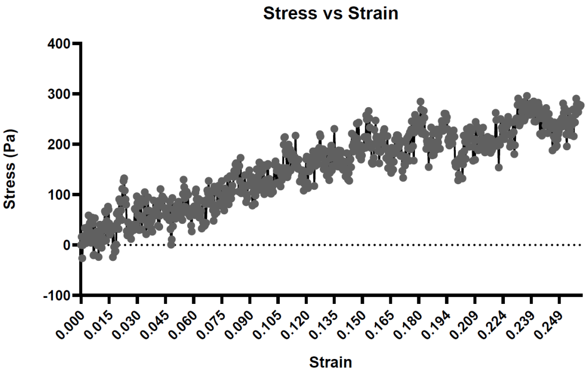

Figure S9: **Representative stress vs strain curve obtained by rheology measurements**

Recellularization

Although CCAOs were grown on dNECM (n=1), besides noticing cellular proliferation, due to time, no further analysis were done due to time constraints (Fig. S14).

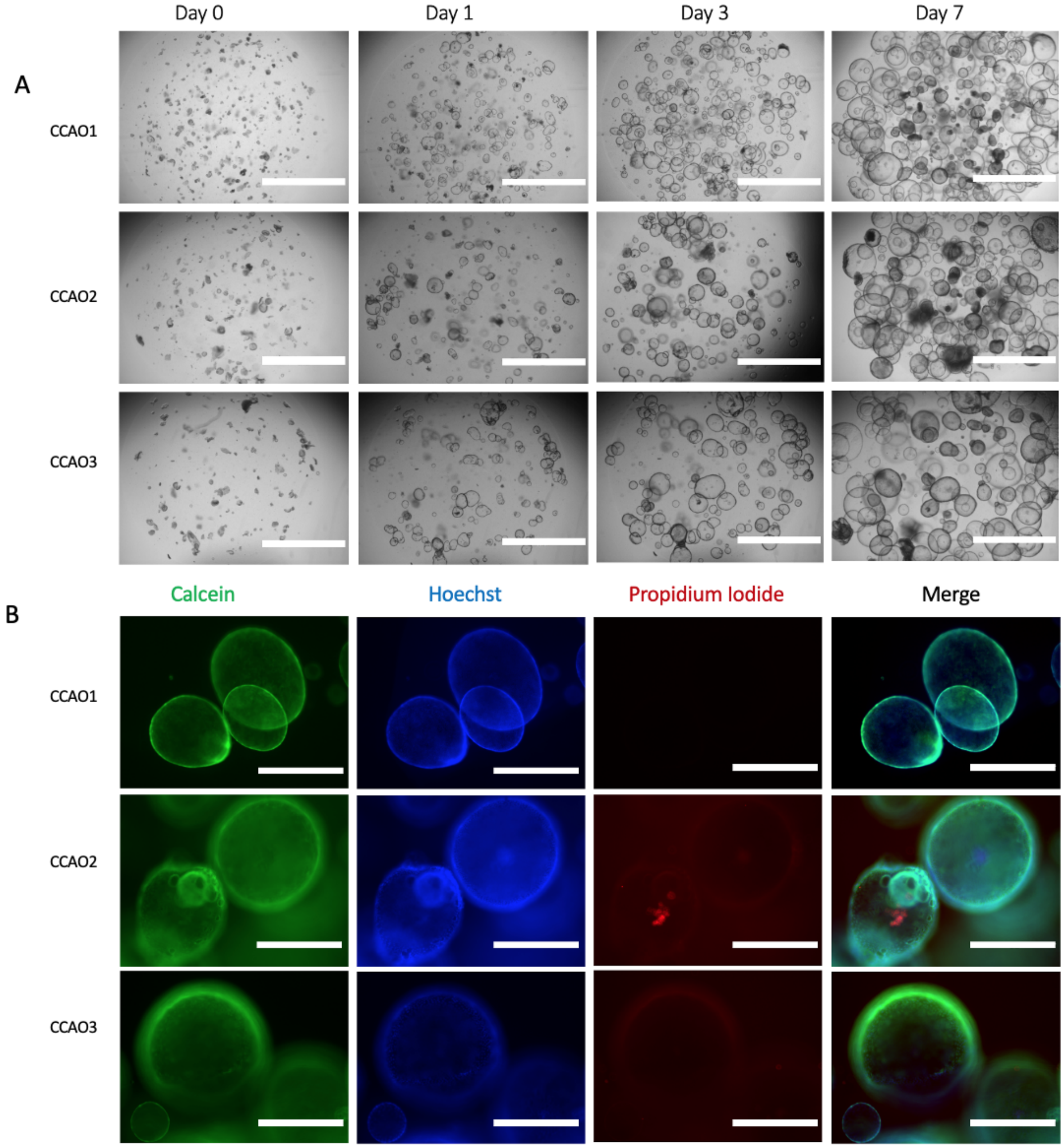

Figure S10: **Expansion and viability of CCAOs. A)** Bright field microscopy images of CCAOs (n=3), growth from day 0 until day 7 after splitting. Scale bars indicate 2000 μm. **B)** Images of live/dead staining of CCAOs grown in BME, showing their viability. Calcein (green) represents live cells, PI (red) represents dead cells and Hoechst stained all cell nuclei. Scale bar CCAO1 indicates 1000 μm, scale bars CCAO2 and CCAO3 indicate 400 μm.

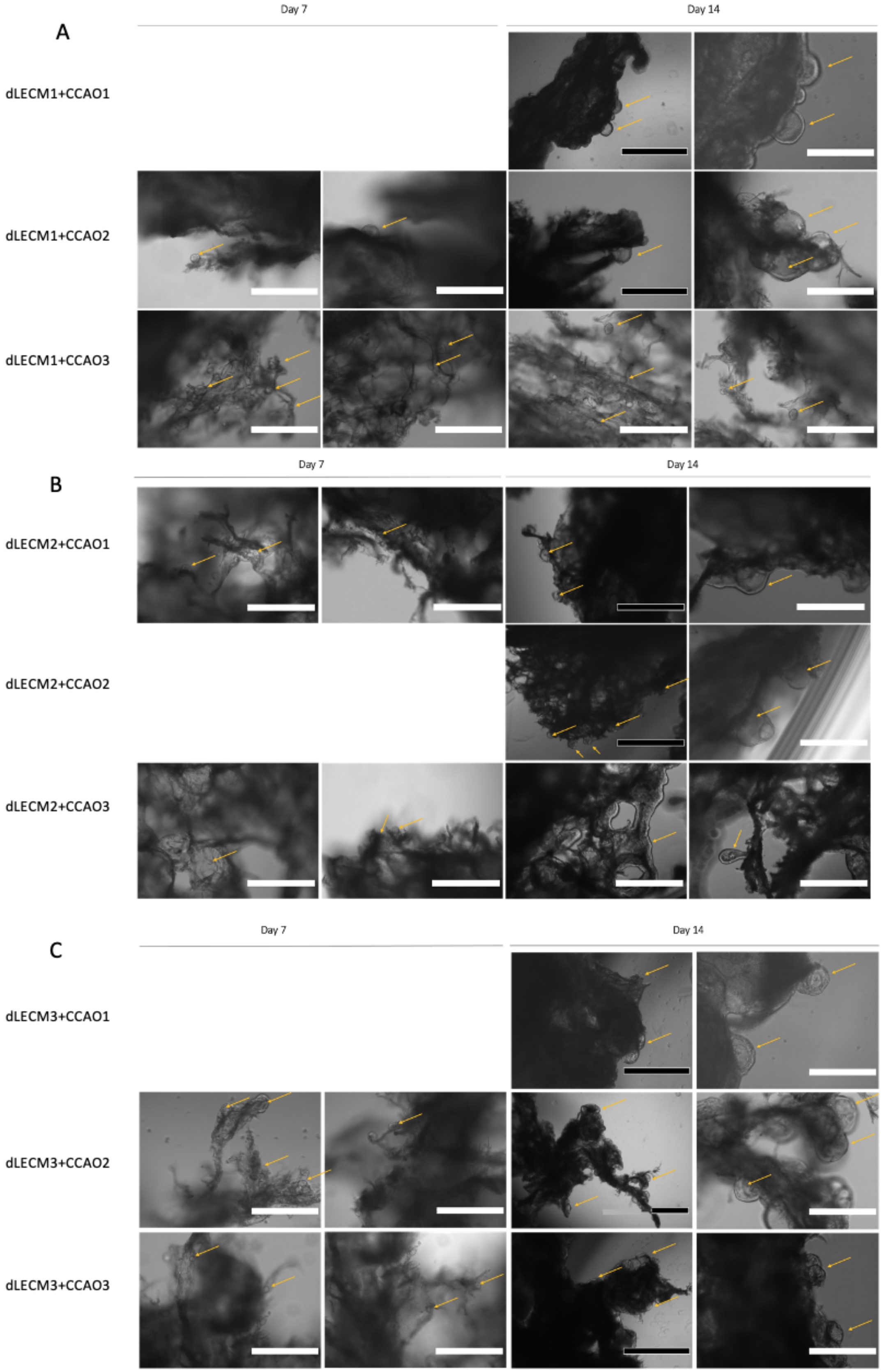

Figure S11: **Additional recellularized dLECM combinations demonstrating adhesion and growth of CCAO in dLECMs. A,B,C)** Bright field microscopy images of CCAOs (n=3) cultured in dLECM (n=3) on day 7 and day 14 after recellularization; (A) dLECM1, (B) dLECM2, (C) dLECM3. Yellow arrows indicate ingrown and adhered organoids. White scale bars indicate 400 μm, black scale bars indicate 1000 μm.

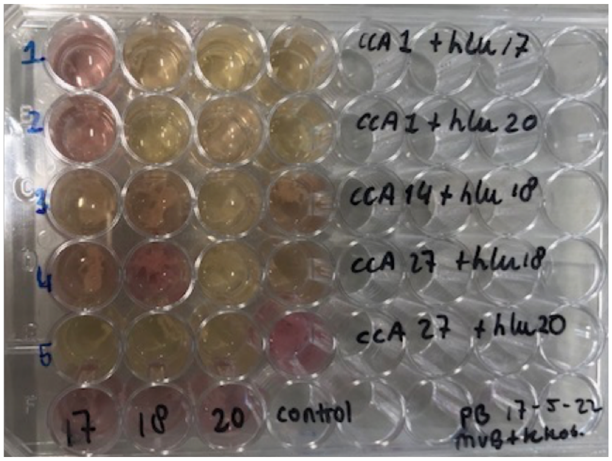

Figure S12: **Variation in color of the expansion medium between biological replicates of recellularized scaffolds (CCAOs + dLECMs) during culturing in 48-wells plate, indicating different growth rates.** CCA14=CCAO2, CCA27=CCAO3, hLu17=dLECM1, hLu18=dLECM2, hLu20=dLECM3.

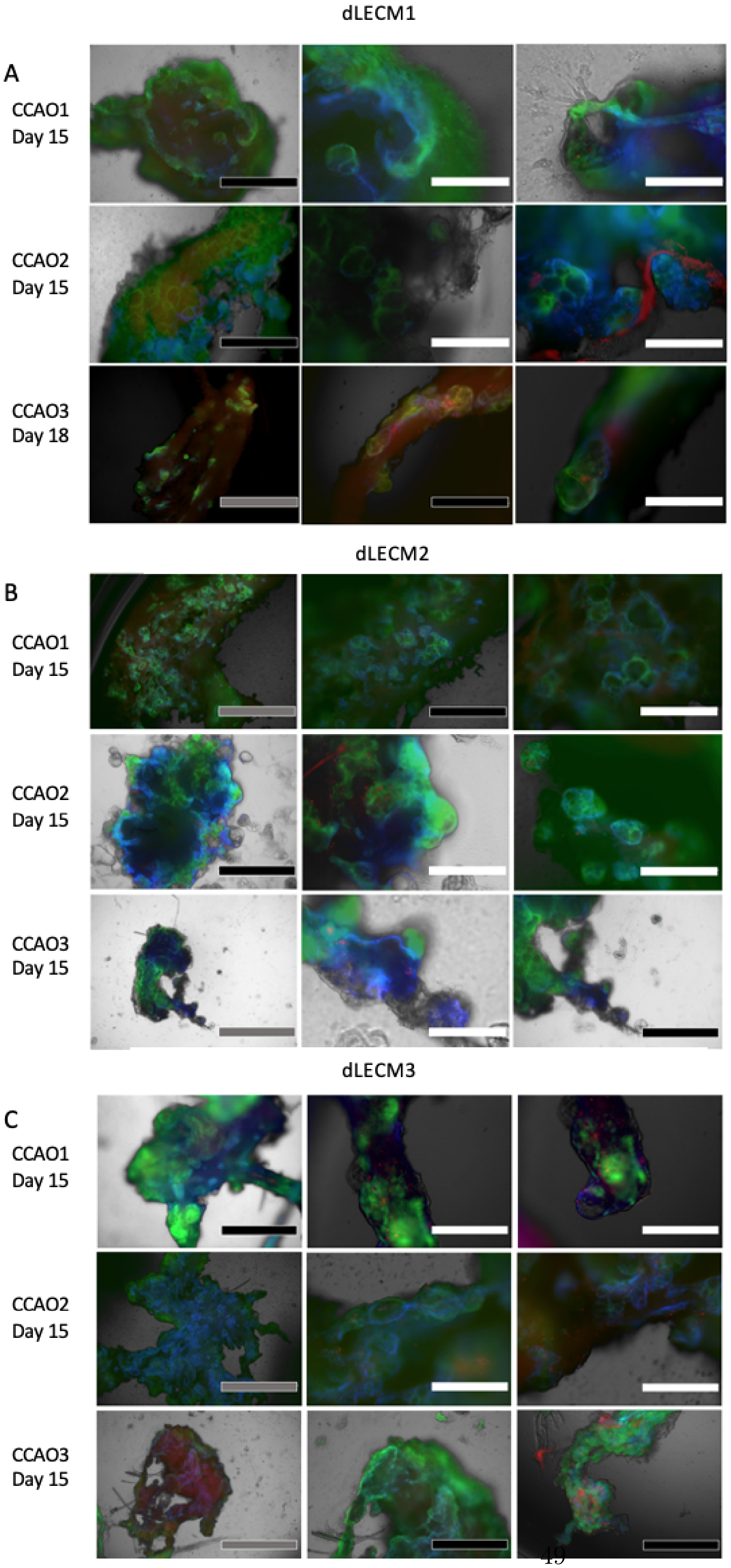

Figure S13: **Live/dead staining of all combinations demonstrating alive CCAOs after recellularization in dLECM.** Merged images of calcein (green) representing live cells, propidium iodide (red) representing dead cells and Hoechst, representing cell nuclei. **(A)** dLECM1, **(B)** dLECM2, **(C)** dLECM3. White scale bars indicate 400 μm, black scale bars indicate 1000 μm, gray scale bars indicate 2000 μm.

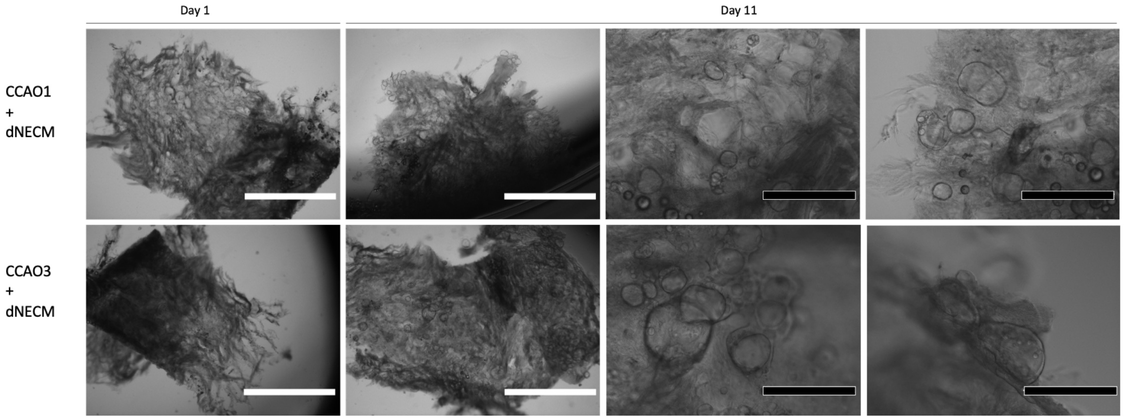

Figure S14: **Recellularized dNECM with CCAOs.** Representative bright field microscopy images of CCAOs cultured in dNECM on day 1 and day 11 after recellularization. The growth of organoids in dNECM5 is visible. White scale bars indicate 2000μm, black scale bars indicate 400μm.

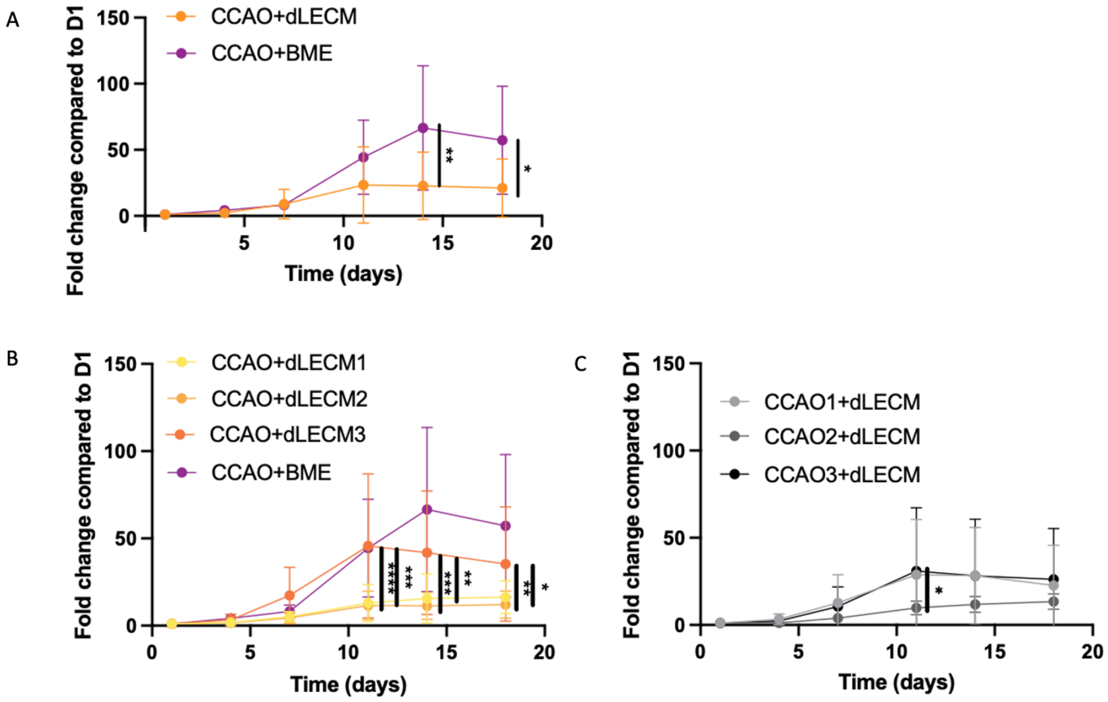

Figure S15: **Increased metabolic activity of recellularized dLECM with CCAOs during 18 days after recellularization**. Two-way ANOVA multiple comparisons statistical test was performed. **A)** Significant differences were present at T=14 (p=0.0018) and T=18 (p=0.0160) days. **B)** Significant differences were present at T=11, T=14 and T=18 between dLECM1 and dLECM3 (p=0.0002, p=0.0039, p=0.0496 respectively) and between dLECM2 and dLECM3 (p<0.0001, p=0.0003, p=0.0073 respectively) **C)** Significant differences were present at T=11 between CCAO2 and CCAO3 (p=0.0331).

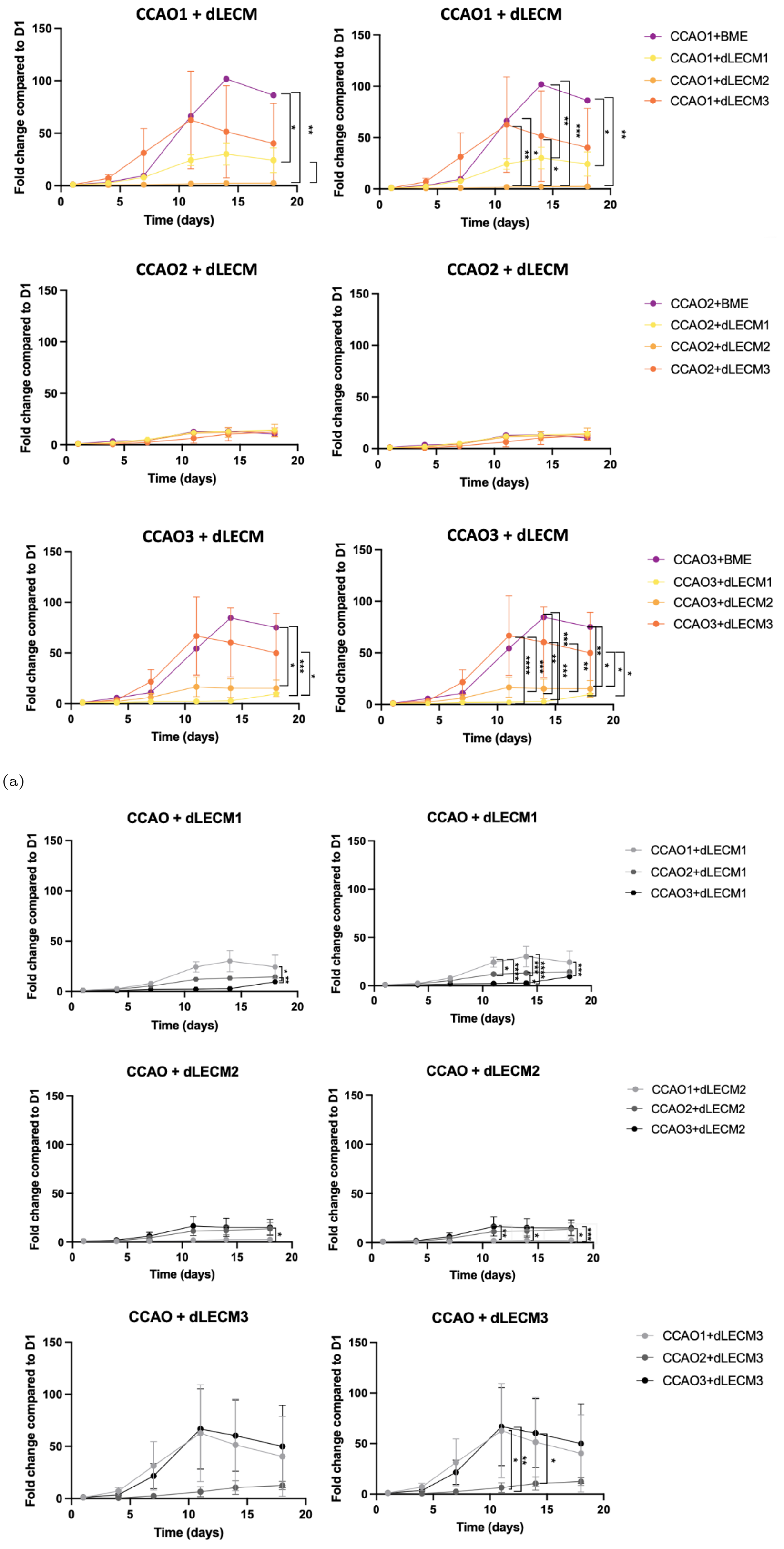

(a)

(b)

Figure S16: **Additional representation of metabolic activity measurements of CCAOs (n=3) cultured in dLECM (n=3)**. In (a) is the data combined considering CCAO lines to compare dLECMs and in (b) considering dLECM donor, to compare CCAO lines. Left column: Two-Way ANOVA test performed, values of 1 line matched by time. Right column: Two-Way ANOVA multiple comparisons test performed.

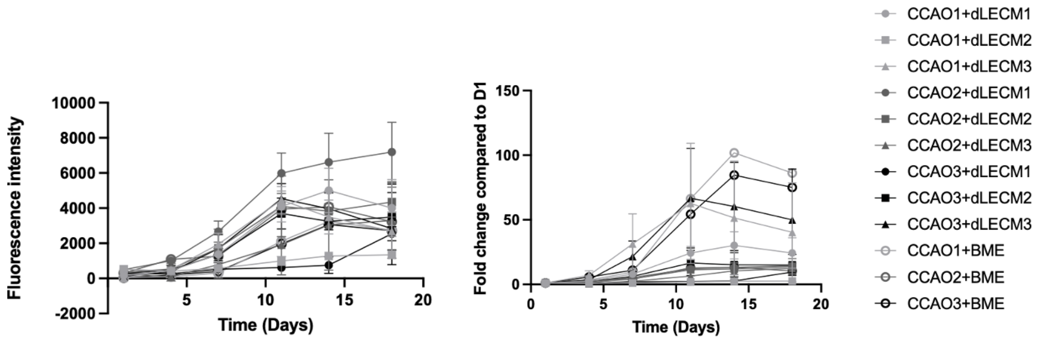

Figure S17: **Additional representation of metabolic activity measurements of recellularized dLECM with CCAOs during 18 days after recellularization.** Left: non normalized data. Right: data is normalized to day 1 (D1).

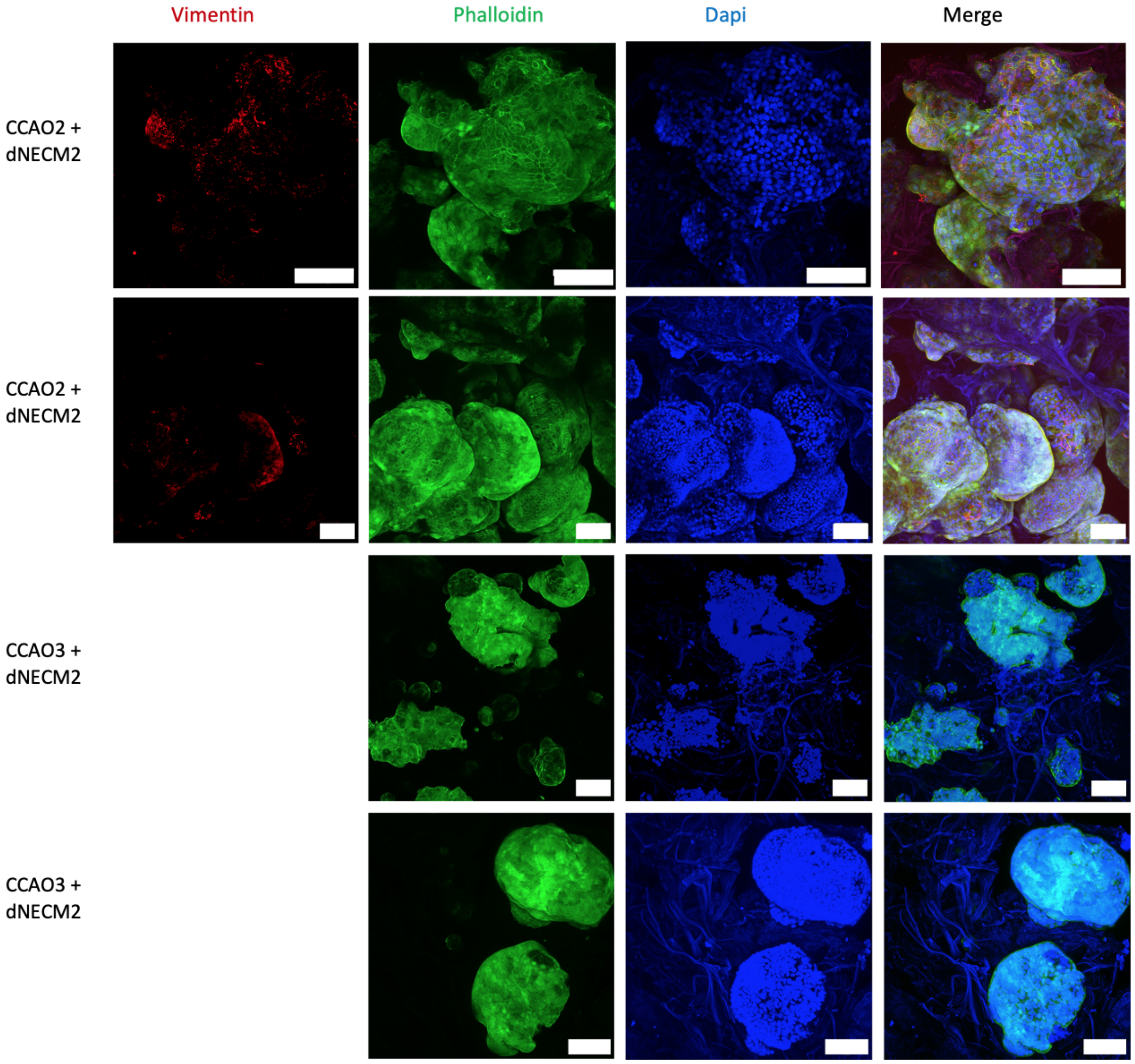

Figure S18: **Whole-mount confocal images for Phalloidin (green), Vimentin (red) and DAPI (blue) for CCAO2 and CCAO3 in dLECM2 at day 18 (CCAO2) and day 19 (CCAO3) after recellularization.** Scale bars indicate 100 μm.